Design of Striplines for the MAX IV and SOLARIS Storage Rings

Olsson, David; Malmgren, Lars; Karlsson, Anders

2017

Document Version:
Publisher's PDF, also known as Version of record

CODEN:LUTEDX/(TEAT-7254)/1-60/(2017)

Design of Striplines for the MAX IV and SOLARIS Storage Rings

David Olsson, Lars Malmgren, and Anders Karlsson

Electromagnetic Theory
Department of Electrical and Information Technology
Lund University
Sweden

(TEAT-7254)/1-60/(2017): D. Olsson *et al.*, Design of Striplines for the MAX IV and SOLARIS Storage Rings

David Olsson
david.olsson@maxiv.lu.se

MAX IV Laboratory
Lund University
P.O. Box 118
SE-221 00 Lund
Sweden

Lars Malmgren
lars.malmgren@maxiv.lu.se

MAX IV Laboratory
Lund University
P.O. Box 118
SE-221 00 Lund
Sweden

Anders Karlsson
anders.karlsson@eit.lth.se

Department of Electrical and Information Technology
Electromagnetic Theory
Lund University
P.O. Box 118
SE-221 00 Lund
Sweden

This is an author produced preprint version as part of a technical report series from the Electromagnetic Theory group at Lund University, Sweden. Homepage `http://www.eit.lth.se/teat`

Editor: Mats Gustafsson

Abstract

MAX IV and SOLARIS are two synchrotron light sources located in Lund and in Krakow, respectively. A stripline is a standard multi-purpose component that is used in many accelerators and consists of one or multiple electrodes. The currents that are induced by the Lorentz contracted fields of the electron beam at the electrodes can be used for beam diagnostics, or one can excite the electrodes in order to manipulate the properties of the beam. The design and initial measurements of the MAX IV/SOLARIS striplines are presented in this report. Different design considerations and possible applications for the striplines are also presented.

Contents

1 Introduction

The MAX IV facility is a national Swedish research facility located in Brunnshög outside Lund [12]. The facility consists of two electron storage rings that are operated at 3 GeV and 1.5 GeV [20], respectively, where the former is optimized for production of high-brilliance hard X-ray synchrotron light, and the latter will produce light in the IR to the soft X-ray spectral range. The rings will be operated with *top-up injections* where the electron losses are compensated by injections at short intervals. The full-energy injector consists of a 39 S-band LINAC structures [21], and will also operate as a driver for a Short Pulse Facility (SPF) where X-ray pulses with durations down to tens of fs are produced. The LINAC might also be the driver for a future Free Electron Laser (FEL) [3], and in this case it is likely that more LINAC structures are added in order to reach higher energies. The 3 GeV ring has recently started delivering light to the first users, while the 1.5 ring is under beam commissioning.

The SOLARIS Synchrotron is a national Polish research facility located in Krakow, and consists of an injector and a storage ring [19]. The storage ring is basically a replica of the MAX IV 1.5 GeV ring. One key difference compared to MAX IV is that the SOLARIS injector has an energy gain of 550 MeV, and the electrons are therefore injected and stored at this energy before the beam energy is increased by the accelerating cavities, and by synchronously increasing the magnetic fields. This process is known as *ramp-up*.

The design parameters of the MAX IV and SOLARIS storage rings are listed in Table 1, and these parameters will be further explained in the following sections. However, the focus in this report is on the design and measurements of the stripline, and its related RF components, that are installed in the MAX IV 3 GeV ring.

Several diagnostic devices are needed for the operation of an electron storage ring. In this paper we describe a stripline can be used for two different types of

Parameter	3 GeV Ring (MAX IV)	1.5 GeV Ring (MAX IV / SOLARIS)
Beam energy	3.0 GeV	1.5 GeV
Maximum beam current	500 mA	500 mA
RMS bunch length	56 mm	56 mm
Main radio frequency	99.931 MHz	99.931 MHz
Harmonic number	176	32
Ring circumference	528 m	96 m
Betatron tune (horizontal/vertical)	42.20/16.28	11.22/3.15
BPM pick-up frequency	500 MHz	500 MHz

Table 1: The design parameters of the MAX IV and SOLARIS storage rings.

beam diagnostics. It can act as a passive device that monitors the longitudinal and transverse motion of the beam. It can also be an active device that excites the beam and by that makes it possible to measure several parameters of the accelerator. Aside from being used as a purely diagnostic device, a stripline can also be used to excite the beam in a way that gives it properties that some users would benefit from or to damp unwanted beam oscillations that are driven by instabilities.

In Section 2, different applications for the stripline are listed. Here, a brief review of the transverse beam dynamics in a circular accelerator is also given. The geometry and manufacturing method of the stripline vacuum chamber is presented in Section 3. An analysis of the transmission line properties and the electromagnetic fields inside the chamber are presented in Section 4. The ability of the stripline to kick the beam and to monitor the motion of the beam are discussed in Section 5 and 6, respectively. When a charged beam propagates inside a vacuum chamber it induces mirror currents on the walls of the chamber. These mirror current generate electromagnetic fields which act back on the beam itself. Such phenomena are known as *collective effects* and are further described in Section 7. In Section 8 the scattering parameters of the manufactured stripline are presented. The design and measurements of an RF distribution network that is feeding the stripline, and an RF receiving network that is monitoring the beam motion are presented in Section 9. Finally, some initial measurements from the commissioning of the MAX IV 3 GeV ring are presented in Section 10 where the beam is excited using the stripline.

2 Applications for the Stripline

A stripline is a multi-purpose tool that can both excite and monitor the electron beam. In this section three possible applications of the stripline are listed.

2.1 Tune measurements

The main purpose of the stripline is to excite the beam during measurements of the betatron tunes. Here, a brief review is given on transverse beam dynamics in

a circular accelerator, and it is shown why monitoring the transverse beam motion provides valuable information about the status of the accelerator.

2.1.1 Transverse Beam Dynamics in a Circular Accelerator

In order to understand the concept tune measurements, one has to understand the basic principles of transverse beam dynamics. In this report, only a brief review is given on the subject. For further reading, [22] and [23] are recommended.

The ideal orbit of a particle with a nominal energy in a circular accelerator is defined by the magnet layout (the *lattice*). The trajectory of a single particle that moves in the vicinity of the orbit can be described by using a co-moving cartesian coordinate system $K(x, y, s)$ whose origin moves along the orbit with the longitudinal position s. $x(s)$ and $y(s)$ are the horizontal and vertical displacement at the longitudinal position s, respectively. For a particle with nominal energy $x(s)$ satisfies Hill's differential equation

$$\frac{\mathrm{d}^2 x(s)}{\mathrm{d}s^2} + k(s)x(s) = 0 \tag{2.1}$$

where $k(s)$ is an L periodic focusing function determined mainly by the quadrupole magnets, and L is the circumference of the ring. The solution to (2.1) is the horizontal oscillating function around the ideal orbit known as the *betatron oscillation*

$$x(s) = \sqrt{\epsilon_x \beta_x(s)}\cos(\psi_x(s) + \varphi_x) \tag{2.2}$$

$$\psi_x(s) = \int_0^s \frac{\mathrm{d}s'}{\beta_x(s')} \tag{2.3}$$

where ϵ_x is the *emittance*, $\beta_x(s)$ is the *beta function*, $\psi_x(s)$ is the *phase advance function*, and φ_x is a constant. Analogously, the vertical displacement from the ideal orbit is given by $y(s) = \sqrt{\epsilon_y \beta_y(s)}\cos(\psi_y(s) + \varphi_y)$. The number of (horizontal/vertical) betatron oscillations performed by a particle travelling once around the ring is called the *betatron tune*, $Q_{x/y}$, and is given by

$$Q_{x/y} = \frac{1}{2\pi}\int_s^{s+L} \frac{\mathrm{d}s'}{\beta_{x/y}(s')} \tag{2.4}$$

There is a chance of resonance growth of the betatron oscillations if Q_x or Q_y are integers or simple fractions. These instabilities are known as *optical resonances*, and they may even result in beam loss. However, it is not sufficient to choose Q_x and Q_y individually so that they are not integers or simple fractions since the field strength in one plane depends on the displacement in the other plane for multipole fields of higher order. A coupled optical resonance has the order $|m| + |n|$, with the resonance condition $mQ_x + nQ_y = p,\ \{m, n, p\} \in \mathbb{Z}$. Generally, the strength of an optical resonance decreases with its order. As seen in Table 1, the optical resonances of the operation points have the order 5 ($m = \pm 5,\ n = 0$) in the 3 GeV ring, and

order 11 ($m = \pm 5,\ n = \pm 6$) in the two 1.5 GeV rings. This pair of values for Q_x and Q_y is called the *working point* of the machine.

The amplitude function $\sqrt{\epsilon_x \beta_x(s)}$ in (2.2) is called the horizontal *beam envelope*. A single particle might have different displacement from its ideal orbit when passing the same longitudinal position in a storage ring. However, the magnitude of this displacement is never greater than the beam envelope, as seen in (2.2). The beta function is determined by the lattice. In (2.2), ϵ_x is a single particle constant of motion, and $\pi\epsilon_x$ is the area of the ellipse of particle motion in the x-x' phase space, where $x' = \mathrm{d}x/\,\mathrm{d}s$. However, a beam consists of many particles oscillating with different amplitudes. One can show that the transverse distributions of an electron beam in a storage ring are nearly Gaussian distributions with rms beam sizes σ_x and σ_y. It is therefore more customary to define ϵ_x as the emittance corresponding to the emittance of electrons travelling at exactly one STD, σ_x, from the ideal orbit. By doing so, the amplitude function $\sqrt{\epsilon_x \beta_x(s)} = \sigma_x(s)$ can be referred to as the horizontal rms *beam size* at the longitudinal position s. ϵ_x can be seen as the horizontal "temperature" of the beam.

2.1.2 Obtaining the Tunes

When operating the machine, it is vital to monitor its betatron tunes and to confirm that it is operating far away from any strong optical resonances. Deviations from the working point might imply misaligned magnets or drift in the magnet power supplies.

Consider a single particle with charge q that is propagating with velocity v on the design orbit in a circular machine. The charge density $\lambda(t)$ of the particle can be described as a Fourier series of the revolution frequency ω_0

$$\lambda(t) = \frac{q}{v} \sum_{n=-\infty}^{\infty} \delta(t - nT_0) = \frac{q}{L} \sum_{n=-\infty}^{\infty} \cos(n\omega_0 t) \tag{2.5}$$

where T_0 is the revolution period. The transverse dipole moment $d(t)$ of the particle is defined as the product of its charge and its transverse displacement from the orbit, thus the horizontal displacement becomes $d(t) = q \cdot x(t)$. From here on, the horizontal/vertical indices of the parameters listed above are dropped since it should be obvious from the content which index to use. The horizontal displacement of the particle is $x(t) = x_0 + \hat{x}\cos(Q\omega_0 t)$, where x_0 is a constant offset due to a closed orbit distortion. Here, a smooth approximation is applied on the phase advance function in (2.3) where $\psi(s) \approx \frac{2\pi Q}{L} s$. One can measure the displacement at a single point in the machine with, for example, a standard button BPM by combining the signals from two opposite located buttons with a 180° hybrid combiner (see Figure 1). By using this set-up, the obtained signal is proportional to the dipole moment of the particle (higher multipole components are discarded in the analysis). Note that a misalignment of the BPM device results in an additional component to the offset of the measured signal, similar to x_0. However, the measured offset can be rejected by

calibration, and by dropping this term the dipole density becomes

$$d(t) = \frac{q\hat{x}}{L} \sum_{n=-\infty}^{\infty} \cos((n+Q)\omega_0 t) = \frac{q\hat{x}}{L} \left(\cos(Q_f \omega_0 t) + \sum_{n=1}^{\infty} \cos((n \pm Q_f)\omega_0 t) \right) \quad (2.6)$$

where Q_f is the fractional part of Q. Apart from the first term in (2.6) at $Q_f\omega_0$, the spectrum consist of frequency components separated $\pm Q_f\omega_0$ from each harmonic of ω_0. The integer part of Q in the measured signal is however lost which is known as the *stroboscope effect*. One method of measuring the integer part is to perform a position measurement along the machine with the offsets at each BPM rejected by calibration. A small dipole field is then applied somewhere in the machine which results in a a small closed orbit distortion, and the number of betatron oscillations per turn can then be counted by taking the difference between the new orbit and the calibrated orbit.

A particle in a circular machine also performs a longitudinal oscillation, or a *synchrotron oscillation*, due to the gradient of the fields in the accelerating cavities when the particle is accelerated off-crest. This is known as *phase focusing*, and the oscillation occurs around the nominal phase (relative to the phase of the accelerating fields) of an ideal particle known as the the *synchronous phase*. Due to the synchrotron oscillation, the particle receives a different momentum gain every turn when it passes the accelerating cavities. Note that the momentum gain per turn is equal to the momentum loss per turn when the phase of the particle is equal to the synchronous phase. The momentum deviation from the nominal momentum p_0 results in a deviations from the nominal revolution period $T_0 = 2\pi/\omega_0$ which relation is

$$\frac{\mathrm{d}T}{T_0} = \eta_c \frac{\mathrm{d}p}{p_0} \quad (2.7)$$

where η_c is the *phase slip factor*. The momentum deviation also causes a shift in the betatron tune since the L-periodic focusing function $k(s)$ in (2.1) has a different magnitude for a particle with an non-nominal momentum. This tune shift is described by the *chromaticity* of the lattice, and given by

$$\xi = \frac{\mathrm{d}Q/Q_0}{\mathrm{d}p/p_0} \quad (2.8)$$

where Q_0 is the nominal betatron tune.

When including the phase focusing into the transverse spectrum, the dipole moment of a single particle can be written as in (2.9), where J_m is the Bessel function of the first kind with index m, Ω_s is the angular frequency of the synchrotron oscillation, φ is a phase constant, and τ_s is the maximum amplitude of the oscillation of the revolution time [18].

$$d(t) = \frac{q\hat{x}}{L} \sum_{n=-\infty}^{\infty} \sum_{m=-\infty}^{\infty} j^{-m} J_m \left(\left(n + Q - \frac{\xi Q}{\eta_c} \right) \omega_0 \tau_s \right) e^{jm\varphi} e^{j((n+Q)\omega_0 + m\Omega_s)t} \quad (2.9)$$

As seen in (2.9), there is an infinite number of synchrotron satellites at $\pm m\Omega_s$ around the betatron lines that were found in (2.6). All these spectral lines are also amplitude and phase modulated. There will be a momentum spread among the electrons in the beam which results in a spread in their betatron tunes and their revolution frequencies. The spectral lines in (2.9) are therefore smeared out in a signal from a real electron beam. Transverse wakefields (see Section 7) result in a shift of the betatron tunes, which means that the position of the spectral lines also depends on the total stored current. Measurements of the beam spectrum are presented in Section 10.

Since the individual electrons also oscillate with different phases, they all perform betatron oscillations around the ideal orbit incoherently. Therefore, in order to measure the betatron tunes one has to excite the beam so that the electrons perform transverse oscillations coherently. This excitation can be made by applying an external driving force to the beam (via for example the stripline), or the beam can be excited by itself due to an instability. The latter case is undesired, and will not be considered in this report. In the 3 GeV ring, three different methods of exciting transverse oscillations and measuring the betatron tunes are implemented.

The first method includes the stripline which excites the beam when it is swept with a sinusoidal signal. The transverse beam position is then monitored by a button BPM where the differential signals between opposite located buttons are measured. Figure 1 shows a simplified illustration of the measurement set-up. A more detailed overview of the RF distribution in the measurement set-up is presented in Section 9. The frequency of the exciting signal is generated by the tracking generator of a spectrum analyzer, and the differential signal at the BPM is monitored by the same instrument. Coherent transverse oscillations are excited when the frequency of the tracking generator is close to the frequency components of the Fourier series in (2.9), and are therefore displayed as spectrum lines by the spectrum analyzer.

In the second method, the beam is excited by a fast transverse kick which has a duration that is less than the revolution period of a bunch. For this purpose, fast pinger magnets are installed in the rings that can kick the beam both in the horizontal and vertical plane. The beam position is then measured at the positions of the button BPMs along the ring. This method is not as accurate as the first method.

A third method is to use the bunch-by-bunch feedback system. Here, an external excitation signal is swept in the vicinity of the betatron frequency (just as in the first method), and the beam spectrum is then obtained as an FFT of the signal from a single button BPM. The bunch-by-bunch feedback system is described in [16].

2.2 Pick-up Device

The stripline will intercept fractions of the mirror current induced by the electron beam. This results in induced signals at the stipline ports which can be used for estimating the total charge, the transverse and longitudinal motion, and the charge distribution of each ring bucket. Even though the storage ring already has several diagnostics tools such as capacitive buttons (button BPMs), current transformers,

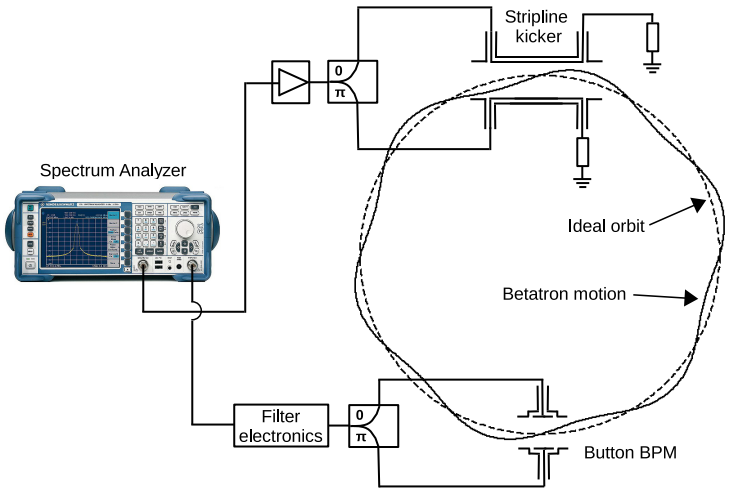

Figure 1: A simplified block diagram that shows the set-up of the betatron tune measurements in FD.

and diagnostic beam lines for these type measurements, the stripline can be used as a complementary pick-up device. The pick-up characteristics of the stripline is investigated in Section 6.

2.3 Feedback Kicker

There are bunch-by-bunch feedback systems installed in both MAX IV storage rings [16]. At the moment, there are no dedicated feedback kickers installed in the 1.5 GeV ring. The stripline that is installed in this ring will therefore operate as a temporary feedback kicker in all three planes when the commissioning of the feedback system starts in this ring during the autumn of 2017.

3 Stripline Geometry

The stripline vacuum chamber consists of a main body, four stripline electrodes, 8 coaxial feedthroughs, and connectors needed for water cooling. A 3D CAD model of the stripline can be seen in Figure 2, and Figure 4 shows the strips and the inner boundaries of the main body in the xy-plane.

Four stripline electrodes are needed since the design target is to construct a device that is able to excite the beam in both transverse planes independently of each other. The stripline electrodes are hereby referred to as "strips", and the complete component is referred to as the "stripline" in this report. The main body and the strips are made of 316LN and 316L, respectively, that are two stainless steel alloys. As seen in Figure 4, tracks are milled in the main body, and the strips are placed inside the cavities. The reason for doing so is to minimize the discontinuity of the inner chamber walls since a beam that passes such discontinuities induces EM

fields that act back on the beam itself which might result in instabilities. More on that in Section 7. The strips are rotated 45 degrees relative to the two transverse planes in order to protect them from synchrotron radiation that is emitted from an upstream dipole magnet. If the synchrotron radiation would hit one of the strips, it becomes heated, and since it is a thin component that is difficult to cool, it might become damaged. Bursts of radiation that hit the strip would also induce noise in the measured signal if the stripline is used as a pick-up device. With the rotation of 45 degrees, the synchrotron radiation hits the main body instead which is the reason why it is cooled by water (see Figure 2). The coaxial feedthroughs that provide the electrical contact between the external feeding network and the strips have N-type connectors and ceramic vacuum insulators. The outer connectors of the feedthroughs are welded to the main body, and the inner conductors are welded to the strips. In order to connect the stripline to the neighboring vacuum chambers, two CF flanges are attached to the upstream and downstream ends of the main body.

In Figure 4, $a = 14.00$ mm, $a_g = 19.04$ mm, $\phi_s = 45.00$ degrees, and $\phi_g = 8.19$ degrees. The length of each strip L is 150 mm (measured between its two welding points to the feedthroughs). The total length of the stripline is 250 mm (flange-to-flange). The dimensions chosen for the stripline are further explained in the following sections.

A total number of four striplines are manufactured; one for each ring in MAX IV and SOLARIS, and one unit is kept as a spare part. One of the completed striplines is shown in Figure 3.

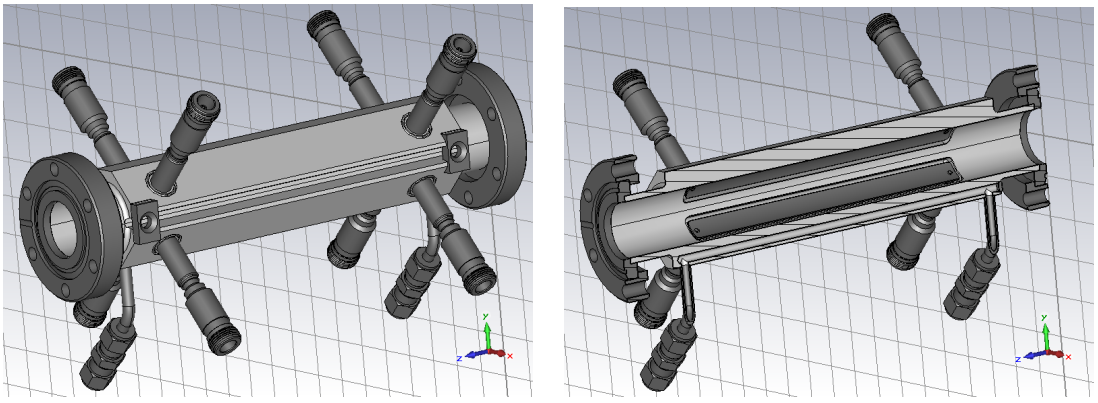

(a) (b)

Figure 2: The CAD model of the stripline, where (a) shows the complete model and (b) shows a cut through in the yz-plane. Note the water cooling channel at the bottom of the main body in (b).

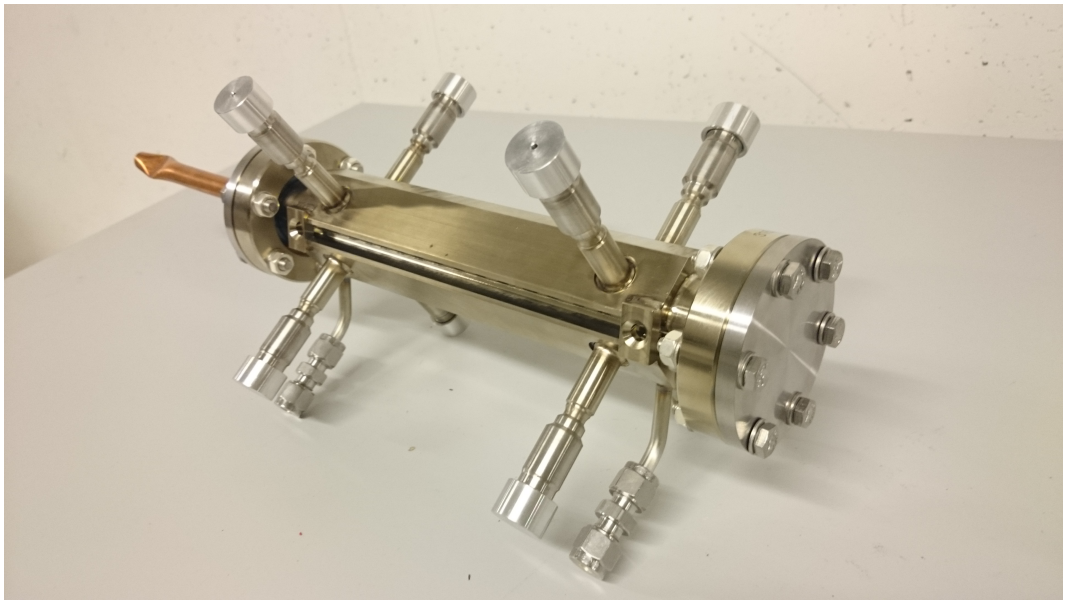

Figure 3: One of the four manufactured striplines.

4 Field and Transmission Line Analysis

The main purpose of the stripline is to excite the beam in the transverse plane. One should be able perform these transverse excitations in the horizontal and vertical planes independently of each other, but also in both planes simultaneously (in the "diagonal plane"). For the beam excitation described above, one needs to operate the stripline in the three different modes that are listed in Table 2. Here, U_n is the applied RF potential to the n:th strip (see Figure 4), where a negative potential is due to a phase shift of 180 degrees compared to the strip with positive potential. The sum mode is not for beam excitation, but describes the potential distribution when a beam that is centered in the beam pipe excites the four strips. This is further explained in Section 6.1. The RF signals are applied to the feedthroughs that are located downstream relative to the electron beam. This is due to the directional properties of a stripline which are explained more in detail in Section 5.1.

4.1 Impedance Matching

Each strip forms a coaxial waveguide, and transmission line theory can therefore be applied in order to obtain the signal along the strip [10]. The analysis is here limited to a transverse cross section of the stripline far away from the feedthroughs. In FD, the voltage propagating along a strip, $U(z)$, is the solution to the transmission line equation

$$\frac{\mathrm{d}^2 U(z)}{\mathrm{d}z^2} - \gamma^2 U(z) = 0 \tag{4.1}$$

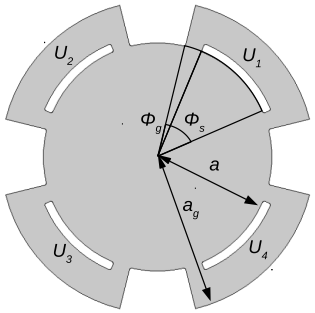

Figure 4: The 2D cross section of the stripline kicker.

Mode of operation	U_1	U_2	U_3	U_4	$Z_s[\Omega]$
Diagonal (d)	V_0	0	$-V_0$	0	50.0
Horizontal (h)	V_0	$-V_0$	$-V_0$	V_0	50.0
Vertical (v)	V_0	V_0	$-V_0$	$-V_0$	50.0
Sum (Σ)	V_0	V_0	V_0	V_0	53.4

Table 2: The modes of operation and their characteristic impedances.

where $\gamma = \sqrt{(R + j\omega L)(G + j\omega C)}$ is the *propagation constant*. R, G, L, and C are the resistance, conductance, inductance and capacitance per unit length, respectively. The analysis is simplified by assuming that the strips are lossfree, thus $R = G = 0$, and phenomena such as attenuation and distortion are therefore not taken into account. Anyway, the losses in the 15 cm strips due to R and G are insignificant below 10 GHz, especially when comparing to the losses introduced by the ceramic vacuum insulators in the feedthroughs. For a lossfree transmission line in vacuum, the *phase velocity* is $v_p = 1/\sqrt{LC} = c_0$. Hence, the propagation constant can now be written as $\gamma = j\omega/c_0 = jk_z$, where k_z is the longitudinal wave number. The voltage $V(z)$ and current $I(z)$ that are propagating along the strip are

$$U(z) = V_0 e^{jk_z z} \tag{4.2}$$

$$I(z) = \frac{V_0}{Z_s} e^{jk_z z} \tag{4.3}$$

since the signal of excitation is travelling in the direction opposite to the electrons (in negative z direction). V_0 is a constant and $Z_s = \sqrt{L/C}$ is the *characteristic impedance* of the strip.

It is necessary that the strips have 50 Ω impedance to minimize mismatch to the feeding system. Since $c_0 = 1/\sqrt{LC}$ and $Z_s = \sqrt{L/C}$, the characteristic impedance of each strip can be obtained as $Z_s = (c_0 C)^{-1}$.

The electric field for the fundamental TEM mode in a coaxial transmission line is obtained by solving the electrostatic field over a transverse cross section (more on that in Section 4.2). C for a strip is given by the electrostatic definition of a capacitor

$$C = \frac{Q_{\text{tot}}}{U} = \frac{1}{U} \oint_{\Gamma} \hat{\boldsymbol{n}} \cdot \boldsymbol{D}(\boldsymbol{r}) \, \mathrm{d}l \tag{4.4}$$

where Q_{tot} and $\boldsymbol{D}(\boldsymbol{r})$ are the total charge per unit length and the electric flux density, respectively. In (4.4), the closed line integration is performed on the curve Γ which is defined by the transverse boundaries of the strip, and $\hat{\boldsymbol{n}}$ is the normal

vector that is directed outward from the strip. Note that Z_s of an individual strip depends on the charge distribution in the surrounding structure, and thereby on the excitation of the other strips. Z_s is obtained numerically in the electrostatic solver in COMSOL Multiphysics for the different modes, and can be seen in Table 2. As seen, there is a slight mismatch in sum mode. COMSOL is a software which can perform numerical simulations within several different disciplines in electrical, mechanical, fluid, and chemical physics [2]. It is also able to solve coupled physics phenomena of different disciplines simultaneously, i.e., pure multiphysics. Besides from using the electrostatic solver in COMSOL, the Frequency Domain solver is used to obtain the S-parameters and the eigenmodes in this report.

Figure 5 shows S_{11} and S_{21} for one strip obtained for the diagonal mode of operation in COMSOL. Even though the strips and the coaxial feedthroughs have impedances close to 50 Ω, there will still be a mismatch in the region where the feedthroughs are welded to the strip. This mismatch becomes more distinctive at higher frequencies as seen from Figure 5. One way to improve the matching is to taper the strips to make the transit region more smooth, but since the main purpose of the stripline is beam excitation and monitoring at frequencies below 1 GHz, this was not implemented. A tapered structure would also complicate the manufacturing process.

4.2 Field Analysis

Solving $\boldsymbol{E}(\boldsymbol{r})$ in Helmholtz equation for the propagating TEM modes is equivalent to solving $\boldsymbol{E}_\perp(\rho,\phi)$ in a two dimensional electrostatic problem. One can therefore analytically obtain the electric scalar potential, $\Phi(\rho,\phi)$, of the (first) propagating TEM modes by solving Laplace equation over a cross section of the stripline. $\boldsymbol{E}_\perp(\rho,\phi)$ is then obtained as $-\nabla\Phi(\rho,\phi)$. The analysis is here limited to the region where $0 \leq \rho \leq a$, and requires that the stripline is evaluated far away from its end gaps. Between the excited strips and the ground at $\rho = a$ the electric field is approximated by $\boldsymbol{E}(a,\phi) = \pm\frac{V_0}{R\phi_g}\hat{\boldsymbol{\phi}}$. By applying the conditions of full azimuthal periodicity, finite $\Phi(\rho=0)$, and the potential at $\rho = a$ described above and in Table 2, one obtains $\Phi(\rho,\phi)$ as the Fourier series in (4.5). The complete expansion of $\Phi(\rho,\phi)$ is presented in Appendix A.

$$\Phi(\rho,\phi) = \sum_{m=1}^{4} \frac{U_m}{\pi}\left(\frac{\phi_s+\phi_g}{2} + \frac{4}{\phi_g}\sum_{n=1}^{\infty}\left(\frac{\rho}{a}\right)^n \frac{\sin\left(n\frac{\phi_g}{2}\right)\sin\left(n\frac{\phi_s+\phi_g}{2}\right)}{n^2}\cos\left(n\left(\phi - \frac{m\pi}{2} + \frac{\pi}{4}\right)\right)\right) \tag{4.5}$$

Figure 6 shows $\Phi(\rho,\phi)$ in the diagonal, vertical, and sum mode obtained in (4.5) (upper figure) together with electrostatic simulations of the same modes in COMSOL (lower figure).

For the modes of operation, it is convenient to define a *transverse geometry factor* $g_\perp = a|\boldsymbol{E}(\rho=0)|/V_0$ in order to compare different designs. Thus, a higher value of $g_\perp$ means a stronger electric field at the origin for a given radius a. The *longitudinal geometry factor* in sum mode is defined as $g_{||} = \Phi(\rho=0)/V_0$. Here, the definitions

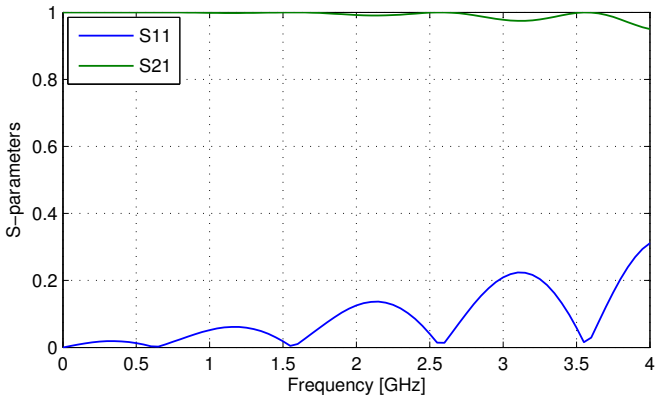

Figure 5: The S-parameters for one strip obtained for the diagonal mode of operation in COMSOL. Note that the vertical scale is linear.

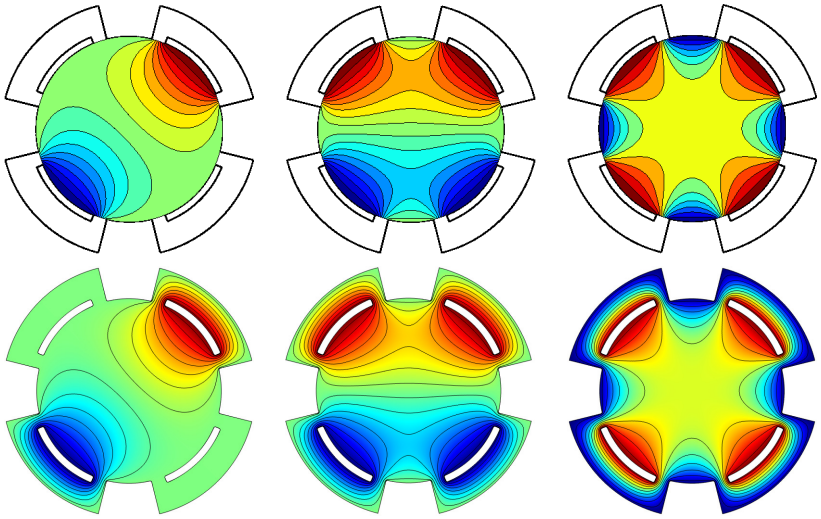

Figure 6: $\Phi(\rho,\phi)$ obtained analytically in (4.5) (upper) and numerically in COMSOL (lower). Here, (from the left) the diagonal, vertical, and sum mode are shown.

of $g_\perp$ and $g_{||}$ described in [6] are used. g for diagonal (d), horizontal/vertical (h/v), and sum mode (Σ) can be derived from (4.5), and are listed in (4.6)-(4.8). For this geometry, $g_{\perp,d} = 0.57$ and $g_{||,\Sigma} = 0.59$. The geometry factors obtained in COMSOL are identical to those obtained analytically when using an accuracy of two decimals. As seen, g_Σ and $g_\perp$ are obtained from the monopole term of $\Phi(\rho,\phi)$ and from the dipole term of $\boldsymbol{E}_\perp(\rho,\phi)$, respectively. Since the beam propagates very close to the z-axis, it is often sufficient to describe the fields in the vicinity of the beam without including any higher order multipole terms in the analysis.

$$g_{\perp,d} = \frac{8}{\phi_g \pi} \sin\left(\frac{\phi_g}{2}\right) \sin\left(\frac{\phi_s + \phi_g}{2}\right) \tag{4.6}$$

$$g_{\perp,h/v} = \sqrt{2} g_{\perp,d} \tag{4.7}$$

$$g_{||,\Sigma} = 2\frac{\phi_s + \phi_g}{\pi} \tag{4.8}$$

The electric and magnetic fields have the same z dependence as the voltages and currents in (4.2) and (4.3). $\boldsymbol{E}(\rho = 0, \phi, z)$ and $\boldsymbol{H}(\rho = 0, \phi, z)$ when the strips are diagonally excited can therefore be written as in (4.9) and (4.10), where the latter is obtained by using Ampere's law .

$$\boldsymbol{E}(\rho = 0, \phi, z) = \frac{V_0 g_{\perp,d}}{a} e^{jk_z z} \left(-\frac{\hat{\boldsymbol{x}} + \hat{\boldsymbol{y}}}{\sqrt{2}} \right) \tag{4.9}$$

$$\boldsymbol{H}(\rho = 0, \phi, z) = \frac{j}{\mu_0 \omega} \nabla \times \boldsymbol{E}(\rho = 0, \phi, z) = \frac{V_0 g_{\perp,d}}{\mu_0 c_0 a} e^{jk_z z} \left(\frac{-\hat{\boldsymbol{x}} + \hat{\boldsymbol{y}}}{\sqrt{2}} \right) \tag{4.10}$$

For the horizontal (vertical) mode of operation, $\boldsymbol{E}(\rho = 0, \phi, z)$ and $\boldsymbol{H}(\rho = 0, \phi, z)$ have the normal vectors $-\hat{\boldsymbol{x}}$ ($\hat{\boldsymbol{y}}$) and $-\hat{\boldsymbol{y}}$ ($-\hat{\boldsymbol{x}}$), respectively. The magnitude of the fields are also a factor $\sqrt{2}$ stronger compared to the diagonal mode of operation due to (4.7).

5 Kick Efficiency

Here, the electromagnetic fields obtained in the previous chapter are used to study how the excited strips affect the beam motion. It will be shown that the deflection of the beam is a function of both the power and frequency of the exciting signals.

5.1 Shunt Impedance and Kick Angle

If the stripline is operating in diagonal mode and the coaxial ports of two opposite strips are excited with voltage signals $\pm V_0 e^{j\omega t}$, the voltage along each strip becomes $U(z,t) = \pm V_0 e^{j(k_z z + \omega t + \varphi)}$, where φ is an arbitrary phase. An ultrarelativistic electron with the velocity $\boldsymbol{v} \approx c_0 \hat{\boldsymbol{z}}$ that propagates inside the excited stripline will obtain a *transverse voltage gain* $V_\perp$ that is given by (5.1). Here, $\boldsymbol{E}(z)$ and $\boldsymbol{B}(z)$ are the on-axis EM fields obtained in (4.9) - (4.10), and $k = \omega/|\boldsymbol{v}| \approx k_z$ is the wavenumber of the beam. Note that $V_\perp$ is not a real voltages strictly speaking, but the transverse work per unit charge since some of the force is a result of the magnetic field. In (5.1), one makes the approximation that $\boldsymbol{E}(z)$ and $\boldsymbol{B}(z)$ only exist in the spatial range of the strips, $-L/2 \leq z \leq L/2$, and have constant magnitudes (but different phases) on that interval. This is not true since there are fringing fields at the ends of the strips, but it gives a good approximation of $V_\perp$. A straight-line approximation is also made. Thus, the deflection provided by the stripline is small. Also note that since $\boldsymbol{v} = c_0 \hat{\boldsymbol{z}}$, $\boldsymbol{E}(z) = \boldsymbol{v} \times \boldsymbol{B}(z)$. On the other hand, if $\boldsymbol{v} = -c_0 \hat{\boldsymbol{z}}$, then $\boldsymbol{E}(z) = -\boldsymbol{v} \times \boldsymbol{B}(z)$, and the particle would obtain no voltage gain. This explains

the directional properties of a stripline.

$$V_\perp = \left(\int_{-L/2}^{L/2} (\boldsymbol{E}(z) + \boldsymbol{v} \times \boldsymbol{B}(z)) e^{j(kz+\varphi)} \, \mathrm{d}z \right)_\perp \approx \frac{2V_0 g_{\perp,d} c_0}{a} e^{j\varphi} \left(\frac{\sin(\omega L/c_0)}{\omega} \right) \tag{5.1}$$

A figure of merit of a stripline is the *transverse shunt impedance* $R_\perp$ which measures its effectiveness to produce a transverse voltage gain for a given input power, P_{rms} . When operating in diagonal mode, two strips are excited and the total rms power becomes $P_{\mathrm{rms}} = 2 \cdot V_0^2/2Z_s$. $R_\perp$ is then given by

$$R_\perp = \frac{V_\perp {V_\perp}^*}{2P_{\mathrm{rms}}} \approx 2Z_s \left(\frac{g_{\perp,d} c_0}{a} \right)^2 \left(\frac{\sin(\omega L/c_0)}{\omega} \right)^2 \tag{5.2}$$

where ${V_\perp}^*$ is the complex conjugate of $V_\perp$. Note that $V_\perp$ depends on the phase φ of the applied RF signal (or equivalent, of the time of arrival of the particle). The product $V_\perp {V_\perp}^*$ is real and independent of φ. In vertical and horizontal mode of operation, the magnitude of $V_\perp$ becomes a factor $\sqrt{2}$ greater compared to the diagonal excitation. However, $R_\perp$ is unchanged since horizontal and vertical mode of operation have four excited strips instead of two, and the required power for the excitation in Table 2 is therefore twice as high. In Figure 7 values obtained from (5.2) are compared to values obtained from COMSOL. At the excitation frequency of 500 MHz, the analytical and numerical values of $R_\perp$ are 1509 Ω and 1457 Ω, respectively. Note that dielectric and ohmic losses in the complete system are not included in the analysis above. As seen from (5.2), $R_\perp$ is maximized if the length of the strips is $L = \lambda/4$. At our BPM monitoring frequency $f = 500$ MHz, $L = 15$ cm is optimum.

Instead of terminating the upstream ports, one can recirculate the RF signal through several strips, as in [17]. That decreases the required power since it increases $R_\perp$. However, this solution is not chosen since it would also make the feeding network (see Section 9.1) more complicated due to the requirements of being able to kick the beam in several transverse planes.

When an electron passes the excited stripline, the transverse voltage gain results in a deflection with a *kick angle* Θ. For small deflections ($\Theta \ll 1$), the maximum kick angle is given by

$$\Theta_{\max} \approx \frac{|eV_\perp|}{W} = \frac{|e|\sqrt{2R_\perp P_{\mathrm{rms}}}}{W} \tag{5.3}$$

where W and e are the energy and charge of the electron, respectively.

6 Pick-up Characteristics

As mention above, the stripline can be used for monitoring several properties of the beam, and the pick-up characteristics are presented in this section. Both the transient response in TD and the response in FD are studied.

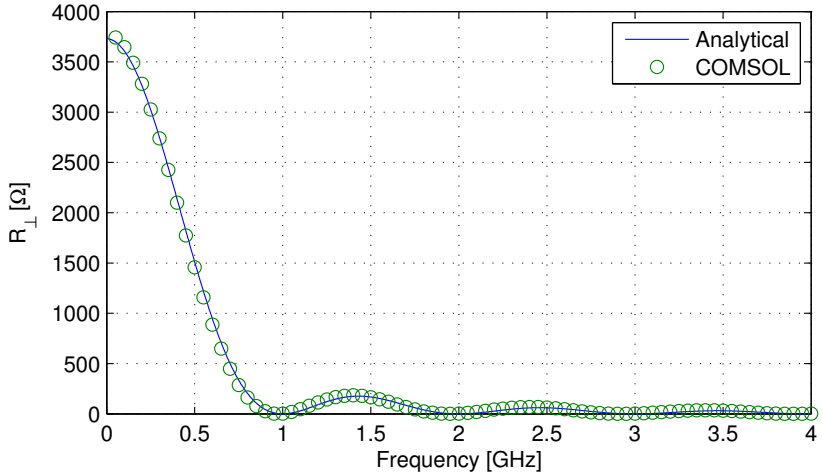

Figure 7: $R_\perp$ obtained from (5.2), and numerically in COMSOL.

6.1 Longitudinal

An electron bunch that propagates inside a vacuum chamber induces image currents on the chamber walls. Due to relativistic effects the EM field of an ultra-relativistic particle is confined to a sector in the transverse direction with angle $\gamma^{-1} = \sqrt{1-(v/c_0)^2}$. The longitudinal distribution of the image currents is therefore approximately the same as for the bunch itself. When a bunch with the current distribution $i_b(t)$ reaches the upstream gap of the stripline at $t = 0$, current pulses are induced on the strips. The intercepted mirror current at each strip is $i_b(t)g_{||,\Sigma}/4$, and it sees an impedance of $Z_s/2$ since the strip consists of two parallel port terminations of Z_s. Hence, the current pulse splits into two equal parts, where the first part propagates to the upstream port, and the second part propagates along the strip where it reaches the downstream port at $t = L/c_0$. When the bunch reaches the downstream end of the stripline at $t = L/c_0$, a negative current pulse is induced. This pulse also splits into two equal parts that propagate in two different directions toward the two terminations. However, the new pulse that propagates to the downstream termination cancels the pulse that was induced at the upstream port at $t = 0$ since they have different polarities. The second half of the new pulse reaches the upstream port at $t = 2L/c_0$. Hence, an ideal stripline BPM is a directional device, where a bi-polar pulse whose two lobes are separated by $t = 2L/c_0$ are induced at the upstream port, and where no signal is induced at the downstream port. Figure 8 shows a circuit model of a strip. The induced voltage, $u_{\text{port}}(t)$, at a single upstream port is given by (6.1). Note that this circuit model is an approximation and requires that the strips are perfectly matched to the external loads. We will therefore from here on assume that $Z_s = Z_L$ in the analysis. This approximation is quite accurate in the lower frequency region. For higher frequencies the characteristic impedance Z_s of the strips may deviate from Z_L, depending on the how the strips are excited. The circuit model approximation is also not valid when reaching the first trapped eigenmodes of the structure itself.

In storage rings, it is often more convenient to express the pick-up characteristics of a device in terms of a *transfer impedance* in FD. Thus, one set the beam current to $i_b(t) = I_b e^{j\omega t}$ and defines the *longitudinal transfer impedance* $Z_p(\omega)$ as the ratio of the induced voltage to the beam current. (6.2) shows $Z_p(\omega)$ where the induced voltage is obtained from the combined signal of the four upstream ports (note that $Z_p(\omega)$ can also be defined from the voltage at a single upstream port and is then a factor 2 lower).

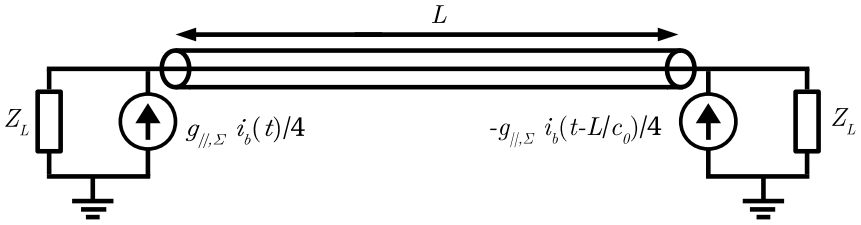

Figure 8: Circuit model of a strip.

$$u_{\text{port}}(t) = \frac{1}{2} Z_s \frac{g_{||,\Sigma}}{4} \left(i_b(t) - i_b(t - 2L/c_0) \right) \tag{6.1}$$

$$Z_p(\omega) = \frac{Z_s g_{||,\Sigma}}{2} e^{j(\pi/2 - \omega L/c_0)} \sin\left(\frac{\omega L}{c_0}\right) \tag{6.2}$$

6.2 Transverse

The induced voltage at an upstream port due to a beam with a offset relative to the z-axis can also be calculated. If the offset is diagonal ($x_{\text{offset}} = y_{\text{offset}}$), an additional dipole field is induced in the structure as in Figure 6 (left). Of course, other higher order fields are also induced, but they can be neglected in a first order approximation for small beam offsets. The induced voltage at the upstream ports of two opposite strips that are located in the same plane as the beam displacement can now be written as

$$u_{\text{port}}(t) = \frac{1}{2} Z_s \left(\frac{g_{||,\Sigma}}{4} \pm \frac{g_{\perp,d}}{2a} \Delta r \right) \left(i_b(t) - i_b(t - 2L/c_0) \right) \tag{6.3}$$

where Δr is the magnitude of the diagonal beam displacement. Note that for a small offset, the induced voltage in the two strips that are orthogonal to the beam displacement are still approximately given by (6.1). The *transverse transfer impedance* $Z'_p(\omega)$ can now be written as in (6.4) and defines the sensitivity of the BPM to transverse beam displacements. In this definition, the voltage in the numerator is obtained as the signal difference between the two ports [6]. The unit of $Z'_p(\omega)$ is Ω/m.

$$Z'_p(\omega) = \frac{Z_s g_{\perp,d}}{a\sqrt{2}} e^{j(\pi/2 - \omega L/c_0)} \sin\left(\frac{\omega L}{c_0}\right) \tag{6.4}$$

6.3 Simulations

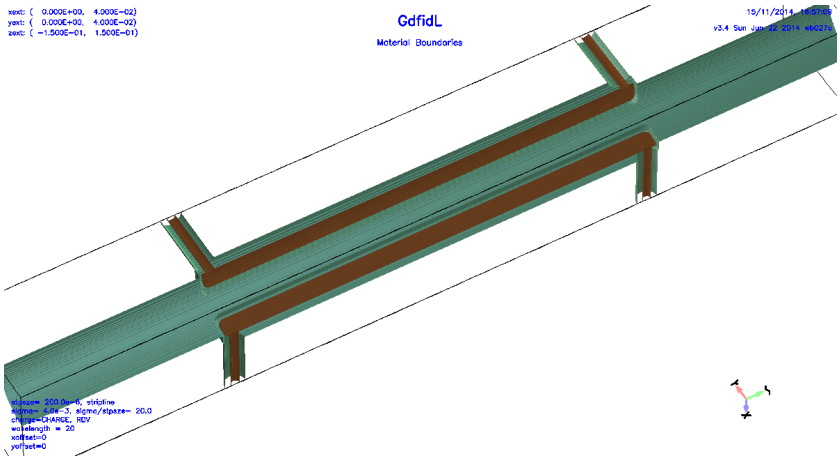

Figure 9: The stripline boundaries in the GdfidL environment when 1/4 of the model is simulated.

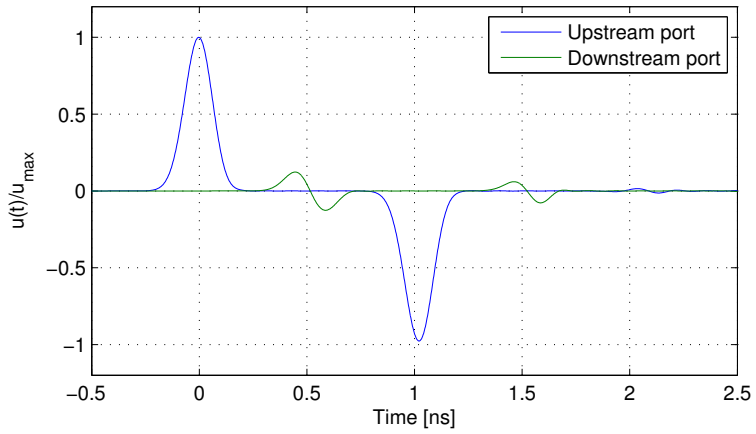

Figure 10: The induced voltage $u(t)$ at an upstream and downstream port obtained in GdfidL. The current source is a Gaussian charge distribution of length $\sigma_z = 20$ mm.

The port response from the electron beam is simulated in GdfidL which is an FDTD based 3D electromagnetic code written in FORTRAN, and developed by Warner Bruns [4]. In these simulations, the source of excitation is an ultra-relativistic Gaussian charge distribution that is propagating through the beam pipe, with and without a transverse displacement. The same simulations are also used to obtain the wake function and the beam impedance in Section 7. GdfidL is also capable of simulating the S-parameters of the ports in TD, and the eigenmodes in FD. However, in this report, COMSOL is used for those simulations. Figure 9 shows the stripline boundaries in the GdfidL environment when 1/4 of the model is simulated.

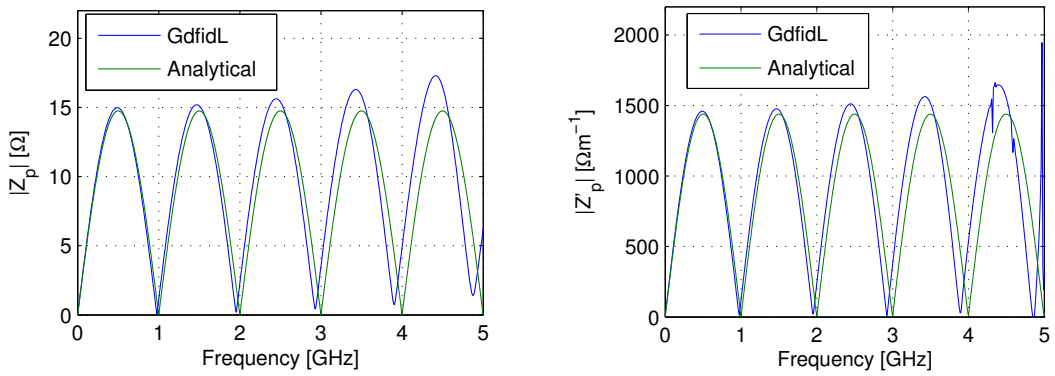

(a) (b)

Figure 11: (a) $Z_p(\omega)$ obtained in GdfidL and in (6.2), (b) $Z'_p(\omega)$ obtained in GdfidL and in (6.4). Note the impact of the trapped eigenmodes in $Z'_p(\omega)$.

Note that only 1/4 of the volume has to be simulated when obtaining $Z_p(\omega)$ since the xz and yz-planes are planes of symmetry where $\hat{\boldsymbol{n}} \times \boldsymbol{H} = 0$.

To illustrate the directional properties of the stripline, the induced voltage in TD at the upstream and downstream ports are plotted in Figure 10. Here, the source of excitation is a Gaussian bunch with $\sigma_z = 20$ mm, and a bi-polar pulse can be seen at the upstream port, while the signal is (almost) cancelled out at the downstream port. As seen, there are some reflected signals at the upstream port around 1 ns after the second lobe arrives. These reflections are caused by mismatch in the regions between the strip and its feedthroughs.

The absolute values of the simulated transfer impedances $|Z_p(\omega)|$ and $|Z'_p(\omega)|$ defined in (6.2) and (6.4) are shown in Figure 11 together with the analytical results. At 500 MHz, which is the operating frequency of the BPM electronics, $|Z_p| = 15.0\ \Omega$ and $|Z'_p| = 1458\ \Omega\text{m}^{-1}$. As expected, the simulated transfer impedances in Figure 11 agree better with the analytical approximations at lower frequencies. The spikes seen above 4 GHz in $|Z'_p(\omega)|$ are caused by trapped transverse eigenmodes. These transverse eigenmodes are investigated further in Section 7.4.2.

7 Collective Effects

In this section, it is studied how the induced mirror currents on the stripline chamber walls act back on the beam itself. Such collective effects are very important to study in an accelerator since they might result in various instabilities.

7.1 Wake Fields

In this section, the particles are assumed to be ultra-relativistic. Such a particle induces *wake fields* in the vacuum structure. Due to causality these fields only exist in a wake behind the exciting particle. It is important to consider the wake fields

in the design of a storage ring. The wake fields can give rise to beam instabilities and unacceptable heating of sensitive components. It might make the storage ring operational only at beam currents levels below the design specifications.

It is often more convenient to study the integrated effect of the wake fields in a structure than the excited EM fields at each point in time and space inside the boundaries of the structure. The integrated effect of the wake field is given by the *wake function*. Consider two test charges q_1 and q travelling parallel to the axis of a vacuum chamber. Both charges have velocity $\boldsymbol{v}$, their transverse displacements from the axis are $\boldsymbol{r}_1$ and $\boldsymbol{r}$. Charge q_1 is the leading charge and is a time τ ahead of q_2. The *longitudinal wake function* $G_{||}(\boldsymbol{r}, \boldsymbol{r}_1, \tau)$ is defined as the energy lost by the trailing charge per unit of both charges q_1 and q as a function of $\boldsymbol{r}$, $\boldsymbol{r}_1$, and τ. Thus, a positive value of $G_{||}$ means a decelerating integrated electric field, and the energy gain of the charge is therefore $\Delta W(\tau) = -qq_1 G_{||}(\tau)$. Here, it is assumed that only the kinetic energy of the charges, and not their trajectories and velocities are altered due to the wake fields excited by the test charge. The wake function has the units V/C.

$$G_{||}(\boldsymbol{r}, \boldsymbol{r}_1, \tau) = -\frac{1}{q_1} \int_{-\infty}^{\infty} E_z(\boldsymbol{r}, \boldsymbol{r}_1, z, \frac{z}{v} + \tau)\, \mathrm{d}z \tag{7.1}$$

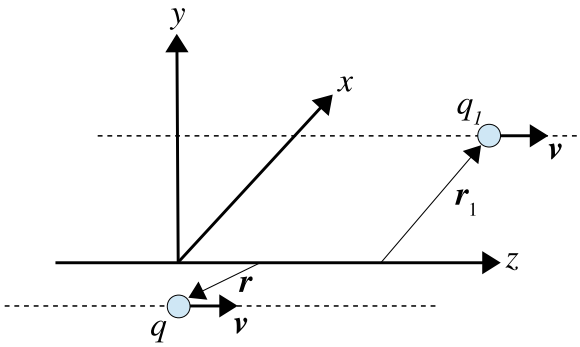

Figure 12: The test and trailing charges with their corresponding coordinates.

Consequently, one can define the *transverse wake function* $\boldsymbol{G}_\perp(\boldsymbol{r}, \tau)$ as in (7.2) which is the integrated transverse force along a straight path at the time τ after the test charge divided by q_1. From here on, it is assumed that the test and the trailing charge have the same offset $\boldsymbol{r}_1 = \boldsymbol{r}$. This is often a valid approximation in most storage rings since the transverse envelope of the beam is much smaller than the cross section of the vacuum chambers.

$$\boldsymbol{G}_\perp(\boldsymbol{r}, \tau) = -\frac{1}{q_1} \int_{-\infty}^{\infty} (\boldsymbol{E}_\perp(\boldsymbol{r}, z, \tau) + \boldsymbol{v} \times \boldsymbol{B}_\perp(\boldsymbol{r}, z, \tau))\, \mathrm{d}z \tag{7.2}$$

One can find different definitions of the transverse wake function in the literature, we prefer (7.2) since it is valid for all structures, with and without any symmetry planes. However, many vacuum structures have symmetry in the xz and in the yz planes. For such structures, $\boldsymbol{G}_\perp(\boldsymbol{r},\tau)$ is zero at the origin, and the most dominant deflecting force is the dipole component of $\boldsymbol{G}_\perp(\boldsymbol{r},\tau)$ which is proportional to the beam displacement. It is therefore common to define the dipole transverse wake function $\boldsymbol{G}'_\perp(\tau)$ as (7.2) divided by the displacement, thus $\boldsymbol{G}'_\perp(\tau) = \boldsymbol{G}_\perp(\boldsymbol{r},\tau)/r$. The unit of $\boldsymbol{G}'_\perp(\tau)$ is [V/Cm].

The wake functions defined in (7.1) and (7.2) are Green functions where the fields are excited by a single point charge. One can also define the wake function, $\boldsymbol{W}(\tau)$, excited by the normalized longitudinal current distribution $\lambda(t)$ of the bunch, where $\int \lambda(t)\,\mathrm{d}t = 1$. The characteristics of $\lambda(t)$ in the storage rings are further discussed in Section 7.2. $\boldsymbol{W}(\tau)$ is then defined as the convolution of $\boldsymbol{G}(\tau)$ and $\lambda(\tau)$, and is given by (7.3) and (7.4). Sometimes in the literature, $W_{||}(\tau)$ and $\boldsymbol{W}'_\perp(\tau)$ are referred to as the longitudinal and the (dipole) transverse wake potential, respectively. Note that $\boldsymbol{W}(\tau) \to \boldsymbol{G}(\tau)$ when $\lambda(t) \to \delta(t)$, where $\delta(t)$ is the Dirac delta distribution.

$$W_{||}(\tau) = \int_0^\infty G_{||}(\tau')\lambda(\tau-\tau')\,\mathrm{d}\tau' \tag{7.3}$$

$$\boldsymbol{W}'_\perp(\tau) = \int_0^\infty \boldsymbol{G}'_\perp(\tau')\lambda(\tau-\tau')\,\mathrm{d}\tau' \tag{7.4}$$

One can obtain the wake function $\boldsymbol{W}(\tau)$ for any arbitrary bunch distribution $\lambda(t)$ once $\boldsymbol{G}(\tau)$ is known. However, most vacuum structures are quite complex, so the wake function has to be obtained numerically. Since the bunch length of the exciting bunch must be a multiple of the mesh size, it is not possible to use $\delta(t)$ as the source of excitation. The wake function is therefore often obtained in a simulation code for a very short charge distribution, and $\boldsymbol{G}(\tau)$ is then approximated as $\boldsymbol{W}(\tau)$. Of course, this limits the accuracy, especially when studying $\boldsymbol{G}(\tau)$ close to the the origin ($\tau \approx 0^+$) [24].

Just like the pick-up characteristics, it is sometimes more convenient to express the wake properties in the FD since it relates the induced beam voltage to the spectrum of the beam current. The *beam impedance*, $\boldsymbol{Z}(\omega)$, is defined as the Fourier transform of the wake function, and its longitudinal and the transverse (dipole) components are given by (7.5) and (7.6), respectively. Unlike the wake function, which is real, the beam impedance is a complex function, where $\mathrm{Re}(Z_{||}(\omega))$ and $\mathrm{Im}(\boldsymbol{Z}'_\perp(\omega))$ are even, and $\mathrm{Im}(Z_{||}(\omega))$ and $\mathrm{Re}(\boldsymbol{Z}'_\perp(\omega))$ are odd functions of ω. The resistive part of the beam impedance relates to the beam voltage that is in phase with the oscillations of the source of excitation, $I(\omega)$, while the reactive part is related to the voltage that is in quadrature with $I(\omega)$. This is the reason for including the imaginary unit j in (7.6). The numerical errors when approximating $\boldsymbol{G}(\tau)$ as $\boldsymbol{W}(\tau)$ in a simulation code does also reduce the accuracy of $\boldsymbol{Z}(\omega)$, which becomes more profound at higher frequencies. $Z_{||}(\omega)$ and $\boldsymbol{Z}'_\perp(\omega)$ have the units [Ω] and [Ω/m],

respectively.

$$Z_{||}(\omega) = \int_0^\infty G_{||}(\tau) e^{-j\omega\tau}\,\mathrm{d}\tau \tag{7.5}$$

$$\boldsymbol{Z}'_{\perp}(\omega) = j\int_0^\infty \boldsymbol{G}'_{\perp}(\tau) e^{-j\omega\tau}\,\mathrm{d}\tau \tag{7.6}$$

The beam impedance that is analysed below is the *geometrical impedance* which only depends on the geometry of structures. Hence, material parameters such as finite conductivity of different materials are not included the analysis. There are definitions of other beam related impedances such as the *resistive wall impedance*, which describes the decelerating field seen by the beam due to the finite conductivity of the structure walls, the *space charge impedance*, which describes the impact of the deflecting forces between the charges in the bunches, and the *synchrotron radiation impedance*, which describes the losses when the bunches move along a curved trajectory. However, these impedances are not treated in this report.

As mentioned, the energy loss of a single trailing charge q is $\Delta W(\tau) = -qq_1 G_{||}(\tau)$. The energy lost for a charge distribution with the total charge q can be written as $\Delta W = -q^2\kappa_{||}$ where $\kappa_{||}$ is called the (longitudinal) *loss factor* and is defined in (7.7). As seen $\kappa_{||}$ depends on the bunch shape and can be defined for a single vacuum component or for the whole accelerator. $\kappa_{||}$ has the unit [V/C]. The power lost in the structure, P_{loss}, is given by (7.8), where I_0 is the total stored current, and f_{RF} is the RF frequency of the accelerating cavities. Note that (7.8) requires that the buckets in the storage ring are uniformly filled, otherwise the expression has to modified. Other "exotic" filling patterns have been discussed for the MAX IV rings, but it is assumed in the calculation below that the buckets are uniformly filled. This power loss has to be compensated by the voltage in the accelerating cavities. However, the majority of the power loss in a storage ring is due to synchrotron radiation in the optics and in the insertion devices (undulators/wigglers). Since the bunch loses energy, some of its energy is transformed to currents and lost in the resistive walls of the structure, and some energy propagates as EM waves to the surrounding structures if the frequency is above or close to the cut-off frequency of the beam pipe. However, it will be shown that in the stripline, almost all of the lost power leaves the structure via the coaxial feedthroughs and dissipates in the 50 Ω terminations.

$$\kappa_{||} = \frac{1}{\pi}\int_0^\infty \mathrm{Re}(Z_{||}(\omega))\lambda(\omega)\lambda^*(\omega)\,\mathrm{d}\omega \tag{7.7}$$

$$P_{\mathrm{loss}} = \frac{I_0^2}{f_{\mathrm{RF}}}\kappa_{||} \tag{7.8}$$

In a similar way, one can define the (dipole) *kick factor* (also called the *transverse loss factor* in the literature), $\boldsymbol{\kappa}'_{\perp}$, as the transverse voltage gain over the total charge in the bunch and the beam displacement which is given by (7.9). Hence, $\boldsymbol{\kappa}'_{\perp}$ has the

units [V/Cm]. The bunch then obtains a transverse kick Θ per displacement each time it passes the component. Θ is given by (7.10). Θ has the unit [rad/m].

$$\boldsymbol{\kappa}'_{\perp} = \frac{1}{\pi}\int_0^{\infty} \mathrm{Im}(\boldsymbol{Z}'_{\perp}(\omega))\lambda^*(\omega)\,\mathrm{d}\omega\lambda(\omega) \tag{7.9}$$

$$\Theta = \frac{eI_0}{f_{\mathrm{RF}}W}|\boldsymbol{\kappa}'_{\perp}| \tag{7.10}$$

The wakefields are simulated in TD for different beam offsets, and the trapped eigenmodes are obtained in FD simulations. The TD simulations are performed in GdfidL, where the wakelength is set to, $s_{\max} = 20$ m, the length of the charge distribution to $\sigma_z = 4$ mm, and the mesh size to 0.2 mm. As mentioned above, a shorter bunch length results in a wake function that is closer to the ideal Green's function, but it increases the computation time and the memory usage. A longer wakelength improves the accuracy of the beam impedance, since it increases the integration span in (7.5) and (7.6). This is most notable in larger structures with many trapped eigenmodes where the excited electromagnetic energy in the structure has a slower decay rate. Note that in [15], the TD simulations were performed in CST Particle Studio. The eigenmode simulations in FD are performed in COMSOL with proper material parameters. Here, the ports can not be terminated with 50 Ω as in the TD simulations, so they must be shorted. Therefore, eigenmodes that couple to the coaxial structure at the ports or to the ends of the beam pipe are unphysical and are therefore discarded.

7.2 Bunch Structure

The MAX IV and SOLARIS storage rings have third harmonic (Landau) cavities installed [1]. Unlike the 100 MHz main accelerating cavities, the Landau cavities operate at 300 MHz and are passive. Thus, their accelerating fields are induced by the electron beam itself by wakefields. The accelerating voltage for one revolution in the rings is given by the superposition of the fields in the main and the Landau cavities, and the result is that the accelerating voltage gradient seen by the beam is flattened out when the fields from the Landau cavities are added. This causes a longitudinal bunch lengthening, which decreases the charge density in the bunches. The current distribution, $i(s)$, within each bunch in a storage ring with third order harmonic cavities has a quartic distribution when operating with a flat potential, and is given by

$$i(s) = \frac{4\pi\sqrt{2\pi}}{\sqrt{2}\Gamma^2(1/4)}\frac{RI_0}{h\sigma_z}e^{-\frac{2\pi^2}{\Gamma(1/4)}\left(\frac{s}{\sigma_z}\right)^4} \tag{7.11}$$

where Γ is the gamma function, and $s = \tau/c_0$ is the distance behind the bunch center [8]. R, I_0, h, and σ_z are the radius of the ring, the average ring current, the harmonic number, and the rms bunch length after the bunch lengthening, respectively (see Table 1). Without the Landau cavities installed, the bunch shape would be close to

Gaussian with $\sigma_z = 12$ mm instead of quartic with $\sigma_z = 56$ mm. Figure 13 shows the current distribution λ in TD and in FD, with and without the Landau cavities in operation. The main advantages of the bunch lengthening are; reduced Touschek scattering, reduced intrabeam scattering, increased longitudinal tune spread, and that it decouples the bunch spectrum from the high-frequency part of the impedance spectrum of the machine.

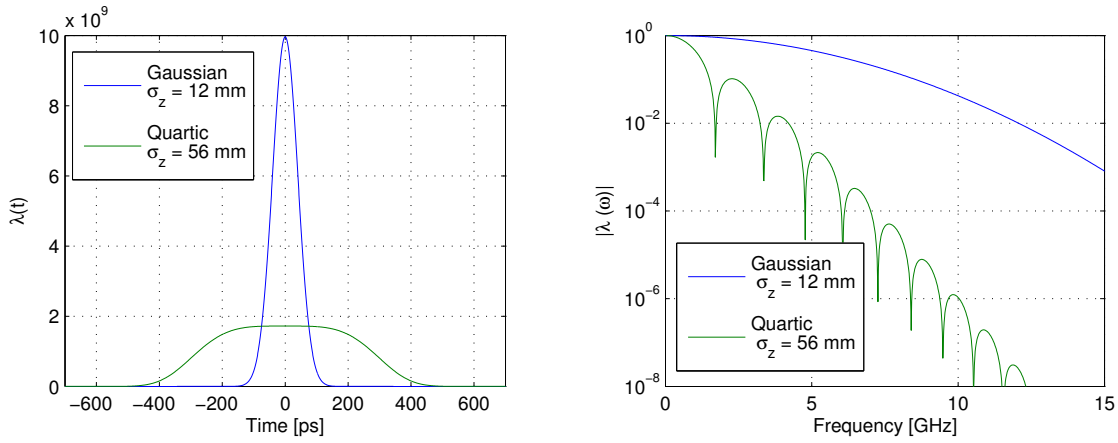

(a) (b)

Figure 13: The normalized current distribution λ in TD (a) and in FD (b), with and without the Landau cavities in operation.

As mentioned in Section 2.1.1, the beam performs transverse betatron oscillations around a closed ideal orbit, which is described by (2.2). When two electrons collide, their transverse momenta can be transformed into longitudinal momenta. If the electrons after the collision have longitudinal momenta that are outside the window of the longitudinal momentum acceptance in the RF-bucket, they are lost. This is called the *Touschek scattering* and is the limiting factor of the stored electron beam life time in modern storage ring. While Touschek scattering describes a process of collisions that result in an immediate beam loss, there are other collisions where the exchange of momenta is too small to result in beam loss. This is called *intrabeam scattering* (IBS). Longitudinal collisions can also result in a transformation of longitudinal momenta into transverse momenta. The result is IBS since the ratio of the longitudinal momenta of the synchrotron motion to the transverse momentum acceptance is too small for beam loss. IBS is a rather slow process and results in higher equilibrium emittance [22]. The increase in emittance due to IBS can be significant for ultra-low emittance storage rings such as the MAX IV 3 GeV ring [20]. By lengthening the bunches, their charge density decrease, and thereby the effects of Touschek and intrabeam scattering.

The spread of the synchrotron tune among the electrons within each bunch increases when the bunches are elongated. This tune spread increases with the nonlinearity of the total RF voltage seen by the bunches. The tune spread has a damping effect on coupled-bunch mode instabilities that are explained more in detail in [16].

As seen in Figure 13 (b), the quartic distribution has a more narrow frequency spectrum compared to the Gaussian one. This shows another advantage of implementing Landau cavities since according to (7.7)-(7.10), only the low frequency part of the impedance spectrum gives a significant contribution to the heat load and kick factor introduced by the vacuum chambers. Hence, the high-frequency part of the machine impedance spectrum, $Z(\omega)$, has little effect on the beam.

7.3 Longitudinal Impedance

7.3.1 Time Domain

As explained in Section 6.1, only a fraction $g_{||,\Sigma}/4$ of the mirror current sees the (geometrical) impedance of each strip if the bunch is propagating on-axis. The result is an induced voltage $U_{\text{port}}(\omega)$ at the upstream gap of the strip which is given by (6.1). This voltage acts back on the beam which sees a potential of $U_b(\omega) = (g_{||,\Sigma}/4)U_{\text{port}}(\omega)$. The total longitudinal beam impedance $Z_{||}(\omega)$ for the four strips is therefore $4U_b(\omega)/I_b(\omega)$ and can be written as

$$Z_{||}(\omega) = \frac{Z_s g_{||,\Sigma}^2}{8}\left(2\sin^2\left(\frac{\omega L}{c_0}\right) + j\sin\left(\frac{2\omega L}{c_0}\right)\right) \tag{7.12}$$

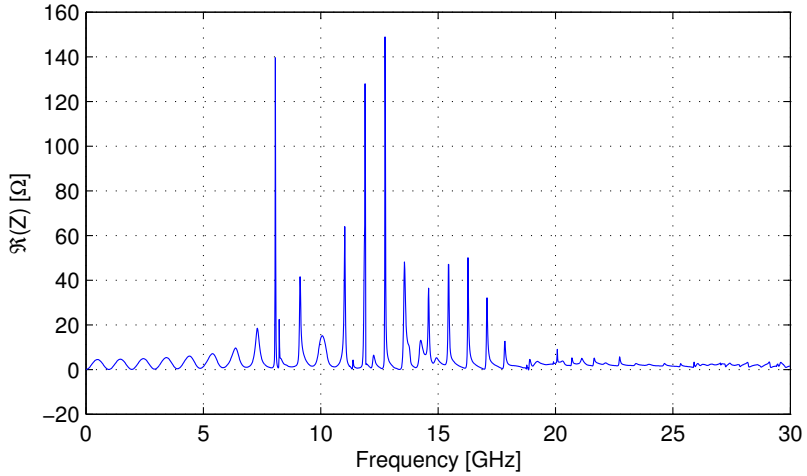

Figure 14: $\text{Re}(Z_{||})$ obtained in GdfidL.

Figure 14 and 15 show $\text{Re}(Z_{||})$ and $\text{Im}(Z_{||})$ up to 30 GHz obtained in GdfidL, and Figure 16 shows the impedance obtained in (7.12) together with the simulation results up to 4 GHz. Here, we also see that the theoretical circuit model has a better agreement with the simulations at low frequencies. When examining Figure 14 and 15, one can distinguish three different regions in the spectrum. In the first region, where $f \lesssim 8$ GHz, the impedance behaves as in the circuit model with a more significant mismatch at higher frequencies. In the second region, where 8 GHz $\lesssim f \lesssim$ 18 GHz, the resonance peaks of trapped and semi propagating modes

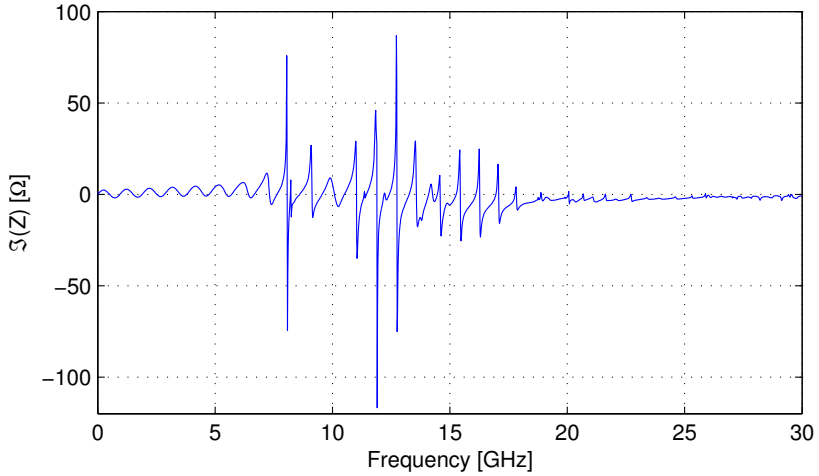

Figure 15: $\mathrm{Im}(Z_{||})$ obtained in GdfidL.

dominate the spectrum. The spectrum in the third region, where $f \gtrsim 18$ GHz, is called the *broad-band impedance* region. In this region, the higher order resonance modes of the structure get denser which results in a smeared out spectrum. Since all these overlapping modes are well above the cut-off frequency of the beam pipe, many of them radiate their power into the surrounding structures which is the explanation to why no significant resonance peaks are found in this region.

By performing an inverted Fourier transform on (7.12), the longitudinal wake function $G_{||}(\tau)$ can be written as in (7.13), where $\delta(\tau)$ is the Dirac delta distribution. Figure 17 shows $G_{||}(s)$ obtained in (7.13) and $W_{||}(s)$ obtained in GdfidL where the 4 mm Gaussian bunch is the source of excitation. Here, the mismatch at higher frequencies is quite notable in form of oscillations, and shows the limitations of the simplified circuit model. One can also see that the second pulse appears at a distance slightly longer than $s = 2L$. This is because L is defined as the distance between the origins of the two coaxial inner conductors that are attached to each strip. Therefore, the "effective length" of each strip is actually somewhat longer. The phenomenon can also be seen in Figure 11 and 16 where the analytical transfer and beam impedances have longer periods in the spectrum compared to when they are obtained in simulations.

$$G_{||}(\tau) = \frac{Z_L g_{||,\Sigma}^2}{8} \left(\delta(\tau) - \delta(\tau - 2L/c_0)\right) \tag{7.13}$$

The loss factors in (7.7) and dissipated power in (7.8) for the 12 mm Gaussian and for the 56 mm quartic distributions are listed in Table 3. As seen, the bunch lengthening that is enabled by the Landau cavities, decreases the power loss by more than a factor 5. Note that when using $\mathrm{Re}(Z_{||})$ from (7.12) to calculate the dissipated power we get $P_{\mathrm{loss}} = 8.42$ W for the 56 mm quartic distribution. When comparing to the other ring components, the dissipated power is quite high for a non-cavity shaped structure. However, most of the power will dissipate in the 50 Ω

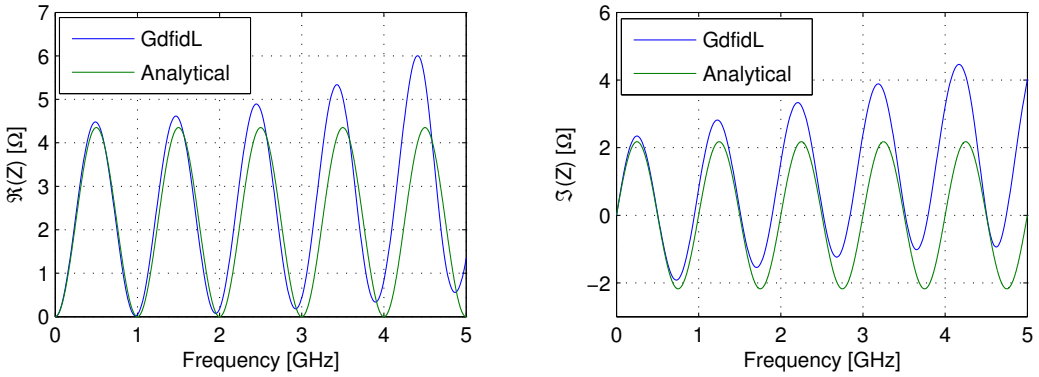

Figure 16: $\mathrm{Re}(Z_{||})$ and $\mathrm{Im}(Z_{||})$ obtained in GdfidL and in (7.12).

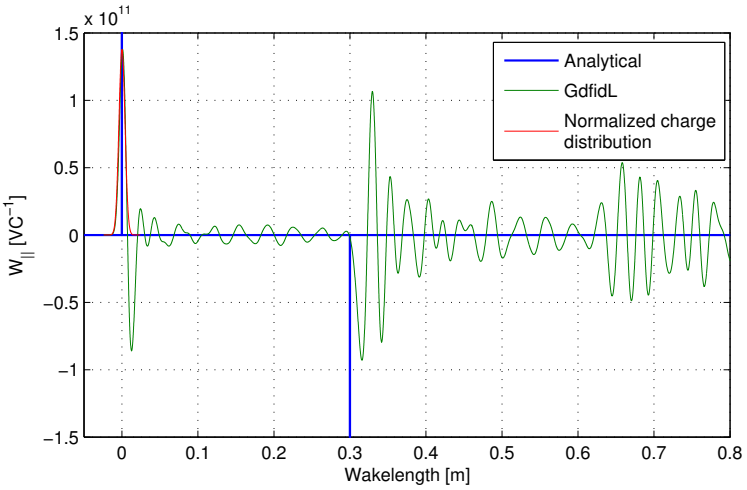

Figure 17: $G_{||}(s)$ obtained in (7.13) and $W_{||}(s)$ obtained in GdfidL. The charge distribution, $\lambda(s)$, normalized to $\max(W_{||}(s))$, is the source of the excitation, and can also be seen.

terminations that are connected to the feedthroughs, and not in the structure itself. Since the longitudinal transfer impedance $Z_p(\omega)$ is known, one can obtain the power lost in the ports P_{port} as

$$P_{\mathrm{port}} = \frac{I_0^2}{f_b \pi} \int_0^\infty \frac{Z_p^2(\omega)}{Z_L} \lambda(\omega)\lambda^*(\omega)\,\mathrm{d}\omega \tag{7.14}$$

By using $Z_p(\omega)$ obtained in GdfidL (see Section 6.1) with the quartic 56 mm distribution, $P_{\mathrm{port}} = 8.14$ W. Thus, the power that is lost in the structure or propagating as EM waves to the surrounding structures is approximately $P_{\mathrm{loss}} - P_{\mathrm{port}} = 10$ mW, assuming that the ports are perfectly matched to 50 Ω. Note that in the ideal circuit model presented above, $P_{\mathrm{loss}} = P_{\mathrm{port}}$.

Guassian $\sigma_z = 12$ mm		Quartic $\sigma_z = 56$ mm	
$\kappa_{\|\|}$ [mV/pC]	P_{loss} [W]	$\kappa_{\|\|}$ [mV/pC]	P_{loss} [W]
18.33	45.86	3.26	8.15

Table 3: The loss factor and dissipated power obtained in GdfidL.

7.3.2 Frequency Domain

As seen in Figure 14, there exist several trapped eigenmodes in the structure. If one uses the parallel RLC-circuit model of the the cavity, one can obtain the longitudinal beam impedance $Z_{||,n}$ of the n:th eigenmode as in (7.15) [24], where $Q_{0,n}$ is the unloaded quality factor of that mode. $R_{\text{s},n}$ is the *longitudinal modal shunt impedance* and is defined as (7.16), where V_n is the voltage obtained by integrating the longitudinal electric field seen by the beam, $V_n = \int E_z(z)e^{jkz}\,\mathrm{d}z$, and V_n^* its complex conjugate. P_{wall} is the power lost in the cavity walls of the corresponding electric field distribution. Since there exist an infinite number of eigenmodes in a cavity, (7.15) is of course only valid in a region close to the particular mode, and requires that the mode is sufficiently separated in frequency from the neighbouring modes. The *modal loss factor* $\kappa_{||,n}$ can then be obtained by using (7.7) and (7.15), and if $Q_{0,n}$ is large, it can be approximated as (7.17). The total loss factor is then obtained as $\kappa_{||} = \Sigma_n \kappa_{||,n}$. In the stripline where almost all of the power dissipates in the port terminations, $\kappa_{||}$ can of course not be obtained as the sum of the modal loss factors. However, for a component with many eigenmodes that have high shunt impedances that are located below the cut-off frequency off the beam pipe, $\kappa_{||}$ obtained in TD and FD are approximately the same. The main and Landau cavities are good examples of such components.

$$Z_{||,n}(\omega) = \frac{R_{\text{s},n}}{1 + jQ_{0,n}(\omega/\omega_{0,n} - \omega_{0,n}/\omega)} \tag{7.15}$$

$$R_{\text{s},n} = \frac{V_n V_n^*}{2P_{\text{wall},n}} \tag{7.16}$$

$$\kappa_{||,n} = \frac{\omega_{0,n}}{2}\left(\frac{R_{\text{s}}}{Q_0}\right)_n \lambda(\omega_{0,n})\lambda^*(\omega_{0,n}) \tag{7.17}$$

Even though $Q_{0,n}$ and $R_{\text{s},n}$ depend on the conductivity of the cavity walls (both terms are inversely proportional to $P_{\text{wall},n}$), the factor $(R_{\text{s}}/Q)_n$ does not. Thus, (7.17) is independent of the material properties, and we are therefore still dealing with the geometrical impedance. In fact, $(R_{\text{s}}/Q)_n$ depends only on the shape of the cavity, and is therefore often called the *geometrical factor* of the cavity.

In the eigenmode simulations, the first trapped longitudinal mode is the TM_{010}-like mode that is found at 8.069 GHz. This mode can also be seen in the TD simulations as the sharp peak at the same frequency in Figure 14. Figure 18 shows $|E_z(\boldsymbol{r})|$ of the mode in the COMSOL environment, and $|E_z(z)|$ in the pipe center of the corresponding mode. As seen, there are two lobes in $|E_z|$ caused by the potential difference between the end gaps of the strips and the surrounding structure. Only

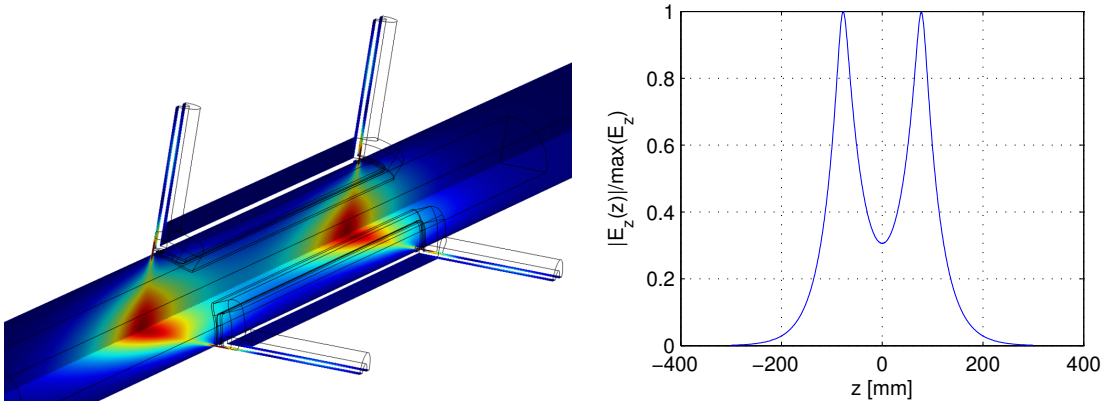

(a) (b)

Figure 18: (a) $|E_z(\boldsymbol{r})|$ of the first longitudinal eigenmode in the COMSOL environment, and (b) $|E_z(x=0, y=0, z)|$ of the same mode.

	f_0 [GHz]	Q_0	R_s [Ω]	$\kappa_{\|\|}$ [mV/pC]	P_{loss} [W]
FD	8.069	939	269	$3.84 \cdot 10^{-9}$	$\mathbf{9.61 \cdot 10^{-9}}$
TD	8.071	-	-	$4.05 \cdot 10^{-9}$	$\mathbf{10.13 \cdot 10^{-9}}$

Table 4: Results obtained for the TM_{010}-like mode in FD and in TD for the 56 mm quartic distribution.

1/4 of the volume is simulated since the boundary conditions of $\boldsymbol{n} \times \boldsymbol{H} = 0$ is true for the mode in the xz and yz planes. Note that it would also be possible to implement a boundary condition of $\boldsymbol{n} \times \boldsymbol{E} = 0$ in the xy plane (at $z = 0$) for this mode and thereby only simulate 1/8 of the volume. Table 4 shows the properties of the mode obtained in FD together with a comparison of the loss factor and dissipated power obtained in TD. In the latter case, $\kappa_{||,n}$ is obtained by integrating $\text{Re}(Z_{||}(\omega))$in the spectrum close to the resonance frequency f_0. As seen, the power lost by the first longitudinal mode is insignificant compared to the power lost in the feedthroughs. The longitudinal mode analysis does not extend further up in frequency since there are many higher-order modes that are semi-propagating and therefore difficult to isolate. Besides, since the other eigenmodes are located even higher up in frequency their contribution to the total power loss is negligible due to the narrow frequency spectrum of $\lambda(\omega)$.

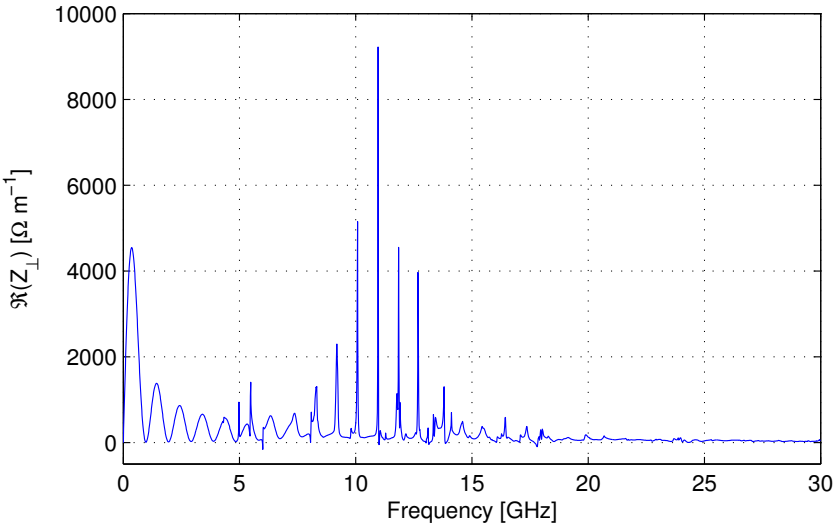

Figure 19: $\mathrm{Re}(Z'_\perp)$ obtained in GdfidL.

7.4 Transverse Impedance

7.4.1 Time Domain

The transverse dipole impedance, $\boldsymbol{Z'}_\perp(\omega)$ is obtained analytically in [14][1]. For a diagonal displacement, $\boldsymbol{Z'}_\perp(\omega)$ becomes

$$\boldsymbol{Z'}_\perp(\omega) = \frac{c_0 Z_s g_{\perp,d}^2}{4a^2}\frac{1}{\omega}\left(2\sin^2\left(\frac{\omega L}{c_0}\right) + j\sin\left(\frac{2\omega L}{c_0}\right)\right)\hat{\boldsymbol{e}}_\perp \tag{7.18}$$

where $\hat{\boldsymbol{e}}_\perp$ is the diagonal unit vector.

Figure 19 and 20 show $\mathrm{Re}(Z_\perp)$ and $\mathrm{Im}(Z_\perp)$ obtained in GdfidL, and Figure 21 shows the analytical impedance obtained in (7.18) together with the simulated one up to 5 GHz. Figure 21 is yet another example on how the accuracy of the circuit model decreases at higher frequencies.

$\boldsymbol{Z'}_\perp(\omega)$ in (7.18) is obtained for a displacement in the diagonal plane. However, in a storage ring, it is often more convenient to express the transverse impedance as Z'_x and Z'_y. If one consider a vertical displacement, $\hat{\boldsymbol{e}}_\perp = \hat{\boldsymbol{y}}$, the induced vertical electric potential is similar to the one in Figure 6 (middle). However, if one compare with the potential induced due to a diagonal displacement in Figure 6 (left), the induced potential at the two upper strips in Figure 6 (middle) is only a factor $1/\sqrt{2}$ compared to the upper right strip in Figure 6 (left) assuming that the magnitude of the horizontal and diagonal displacements are the same. Since the vertical and diagonal geometry factors, $g_{\perp,v}$ and $g_{\perp,d}$, in (4.6)-(4.7) are defined when the strips are held at positive and negative unit potentials, the magnitude of the deflecting electric field in the origin, $|\boldsymbol{E}_\perp|$, is identical for a vertical and for diagonal beam displacement because $(1/\sqrt{2})g_{\perp,v} = g_{\perp,d}$. Hence, the transverse impedance $|\boldsymbol{Z'}_\perp(\omega)|$

[1] In [14], the transverse geometry factor is approximated as $g_{\perp,d} = (4/\pi)\sin(\phi_s/2)$.

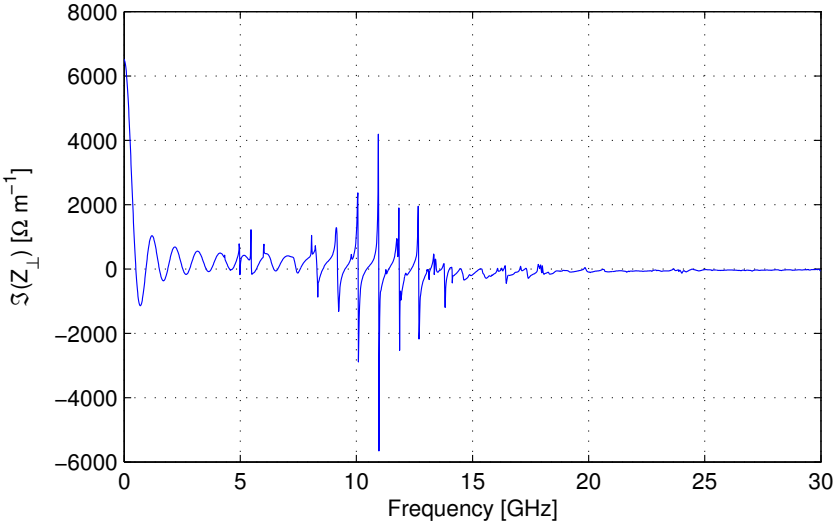

Figure 20: $\mathrm{Im}(Z'_\perp)$ obtained in GdfidL.

Guassian $\sigma_z = 12$ mm		Quartic $\sigma_z = 56$ mm	
$\kappa_\perp$ [mV/pCm]	Θ [μrad/m] (1.5 GeV / 3 GeV)	$\kappa_\perp$ [mV/pCm]	θ [μrad/m] (1.5 GeV / 3 GeV)
4542	15.15 / 7.575	3288	10.97 / 5.483

Table 5: Kick factor $\kappa_\perp$ and kick angles Θ for the 12 mm Gaussian and 56 mm Quartic distributions obtained from the transverse simulations. Θ is listed for energies of 3 GeV and 1.5 GeV.

is identical for a vertical (or horizontal) and a diagonal displacement. Simulations confirm this.

The transverse dipole wake function $G'_\perp(\tau)$ is given by (7.19) and can be obtained by performing an inverted Fourier transform on (7.18) and by using the integral representation of the Heaviside step function $\theta(\tau)$.

$$G'_\perp(\tau) = -\frac{c_0 Z_s g_{\perp,d}^2}{4a^2}\left(\theta(\tau) - \theta\left(\tau - \frac{2L}{c_0}\right)\right) \tag{7.19}$$

Figure 22 shows $G'_\perp(s)$ obtained analytically in (7.19), and $W'_\perp(s)$ obtained in GdfidL, where the source of excitation in the latter is the 4 mm Gaussian test bunch. Note the oscillations around $s = 0.3$ m in $W'_\perp(\tau)$ due to the mismatch explained above.

Table 5 shows the kick factors and kick angles obtained in the TD simulations. Here, Θ is calculated for a uniform filling pattern and $I_{\mathrm{tot}} = 0.5$ A. Note that $\kappa_\perp$ = 3054 mV/pCm for the 56 mm quartic distribution when using the transverse impedance in (7.18).

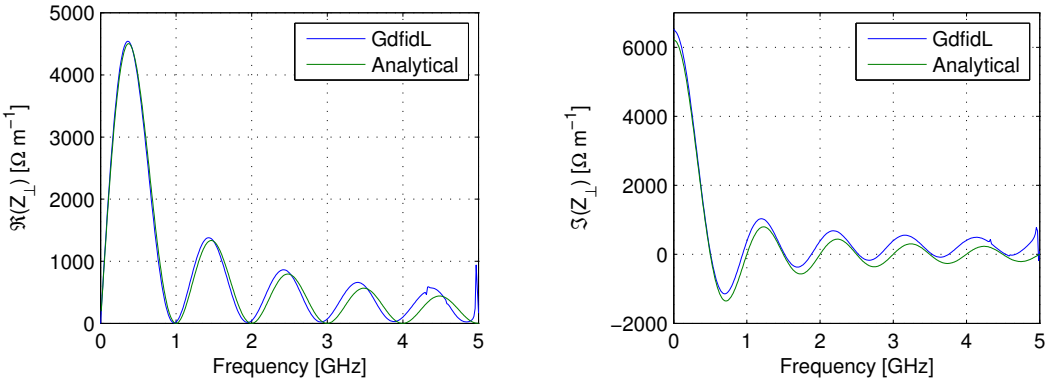

Figure 21: $\mathrm{Re}(Z'_\perp)$ and $\mathrm{Im}(Z'_\perp)$ obtained in GdfidL and in (7.18).

7.4.2 Frequency Domain

There are several trapped TE modes in the structure. These are very similar to those found in a cavity magnetron, and for this reason we adopt the same notation as in [5]. The TE modes have longitudinal magnetic field components in the cavity volumes between the strips and the main chamber. The phase difference of H_z in such a cavity to H_z in one of its neighbouring cavities determines the name of the transverse mode. The $\pi/2$, π, and 0 modes are the fist TE modes that are found in a 2D cross section, and these have indices $m = 1, 2, 3$, respectively. Figure 23 shows $H_z(\boldsymbol{r})$ and $\boldsymbol{E}_\perp(\boldsymbol{r})$ of the mentioned 2D modes in the COMSOL environment, and Table 6 lists their resonance frequencies $f_{\perp,m}$. Note that the $\pi/2$ mode is a degenerate mode, and there are therefore two $\pi/2$ modes with the the same resonance frequency whose transverse electric field are orthogonal to each other.

$f_{\perp,m}$ [GHz]	Index	ID
4.250	$m = 1$	$\pi/2$ (x2)
5.064	$m = 2$	π
6.479	$m = 3$	0

Table 6: The resonance frequencies, $f_{\perp,m}$, of the first three transverse eigenmodes found in a 2D cross section of the stripline.

Since $\boldsymbol{H} \cdot \hat{\boldsymbol{n}} = 0$ at the metallic surfaces in the cavities, we can obtain an approximation of the corresponding 3D modes as

$$f_{m,n} \approx \sqrt{f_{\perp,m}^2 + \left(\frac{nc_0}{2L_c}\right)^2}, \ (m,n) \in \mathbb{Z}^+ \tag{7.20}$$

where $f_{\perp,m}$ is the resonance frequency of the m:th transverse mode found in the 2D cross section. Table 7 lists the 3D modes obtained in COMSOL, and Figure 24 shows $H_z(\boldsymbol{r})$ of the TE_{21} mode (the first π-mode). Note that $\pi/2$-modes where $n > 4$ are not listed since their frequencies are above the cut-off frequency of the

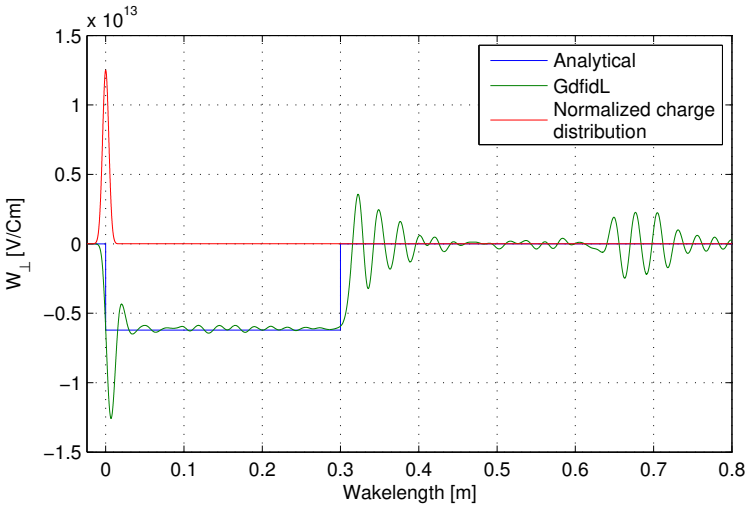

Figure 22: $G'_\perp(s)$ obtained in (7.19) and $W'_\perp(s)$ obtained in GdfidL. The charge distribution, $\lambda(s)$, normalized to $\max(W'_\perp(s))$, which is the source of excitation in the simulation is also included.

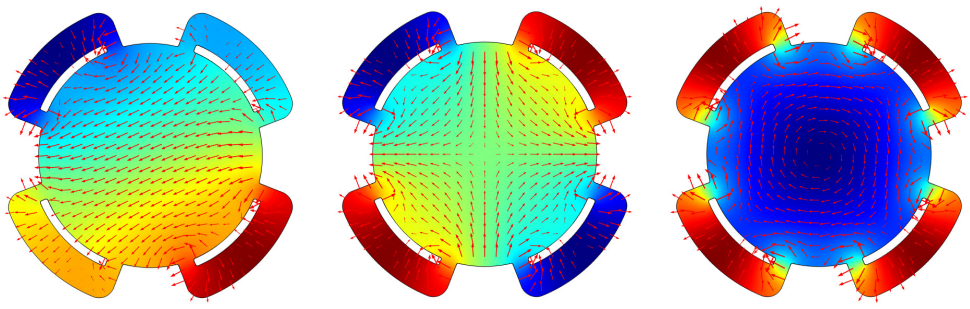

Figure 23: (from left to right) the $\pi/2$, π, and 0 mode in a 2D cross section of the stripline. The color scale shows $H_z(\boldsymbol{r})$, and the red arrows show $\boldsymbol{E}_\perp(\boldsymbol{r})$.

TE_{11} mode of the pipe. Also note that the TE_{11}, TE_{12}, and TE_{13} modes are visible as glitches in Figure 21.

8 Stripline S-parameter Measurements

The purpose of these measurements is to study the impedance matching and to confirm that no severe mismatches exist. The input port of a strip is matched to 50 Ω when the input port of the opposite located strip is excited with a signal that has the same potential but is phase shifted 180° as described in Table 2 and Figure 6 (left). Therefore, it is relevant to produce the same distribution of signal potentials during the measurements. This can be done with a *differential-mode* measurement using a 4-port *Vector Network Analyzer* (VNA).

The most common way of transmitting a signal in transmission lines is by us-

$f_{m,n}$ [GHz]	Q_0	Index	ID
4.336	660	$m = 1, n = 1$	$\pi/2$ (x2)
4.595	612	$m = 1, n = 2$	$\pi/2$ (x2)
4.981	697	$m = 1, n = 3$	$\pi/2$ (x2)
5.136	624	$m = 2, n = 1$	π
5.366	612	$m = 2, n = 2$	π
5.473	736	$m = 1, n = 4$	$\pi/2$ (x2)
5.729	601	$m = 2, n = 3$	π
6.202	594	$m = 2, n = 4$	π
6.529	994	$m = 3, n = 1$	0
6.707	937	$m = 3, n = 2$	0
6.760	595	$m = 2, n = 5$	π
6.996	869	$m = 3, n = 3$	0

Table 7: f_c, Q_0, and indices of the trapped transverse eigenmodes up to 7 GHz obtained in COMSOL.

ing *single-ended* or *unbalanced* transmission lines such as coaxial, microstrip, and coplanar lines. In single-ended transmission lines, the signal is represented as the voltage between the signal conductor and ground. The drawback is that the ground potential might vary along the transmission line due to currents in the ground plane that might interfere with the measured signal. These current can be caused by the external interferences or by the signal itself, and result in potential differences because of the finite conductivity and parasitic inductances in the conductors. Besides from interfering with the signal itself, a single-ended transmission line might also act as an antenna and can therefore interfere other electrical system.

One way of reducing the interference caused by ground currents is to use a *balanced* transmission line with two symmetrical conductors that are separated from ground. The signal in a balanced transmission line in differential-mode is represented as the voltage between the two conductors without using ground as a signal reference. In theory, the potential of the surrounding ground becomes irrelevant for a balanced transmission line. The stripline excited in diagonal mode in Figure 6 (left) is a good example of a balanced transmission line in differential-mode.

Besides from differential-mode signals, *common-mode* signals where the two conductors have the same potentials and phases can also propagate along a balanced transmission line. Common-mode signals are often unwanted, but in an ideal balanced transmission line, a common mode interference would not degrade the signal quality since it is easy to distinguish it from the differential mode signal. However, *cross-mode* conversion between common-mode and differential-mode signals (and vice verse) might exist, which results in interference. This can happen if the symmetry of the two conductors is not perfect. Differential and common-mode are also known as odd and even mode, respectively.

A 4-port VNA can perform *mixed-mode* measurements where the differential, common, and cross-mode S-parameters of a balanced transmission line are obtained by using *modal decomposition* [7]. Here, the four physical VNA ports are represented

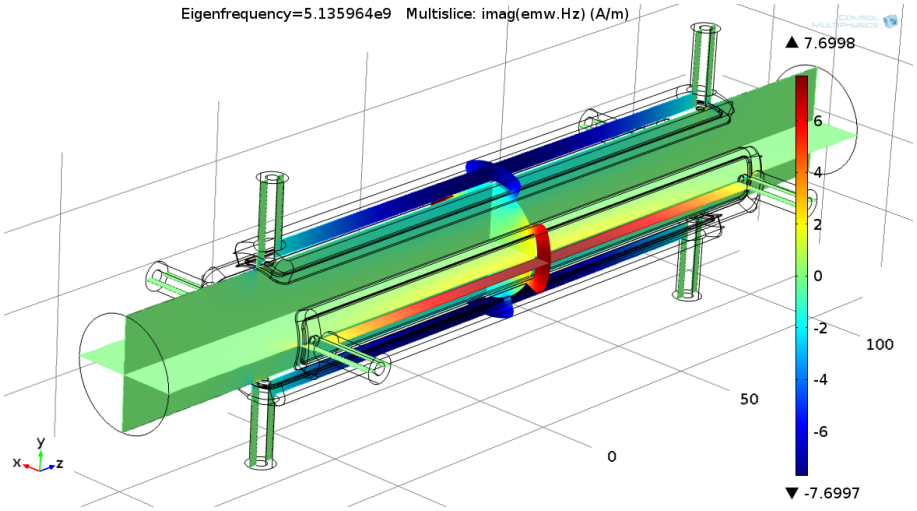

Figure 24: $H_z(\boldsymbol{r})$ (color scale) of the first π-mode ($m = 2,\ n = 1$) in the COMSOL environment.

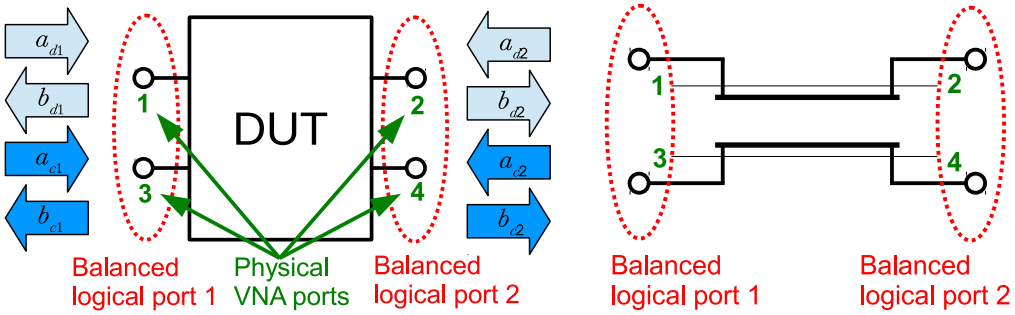

(a) (b)

Figure 25: (a) A physical four-port DUT (Device Under Test) during mixed-mode measurements, and (b) the port configuration during the stripline measurements.

as two logical ports which are shown in Figure 25 (a). The mixed-mode S-matrix is defined as

$$\boldsymbol{S} = \begin{bmatrix} S_{\mathrm{dd11}} & S_{\mathrm{dd12}} & S_{\mathrm{dc11}} & S_{\mathrm{dc12}} \\ S_{\mathrm{dd21}} & S_{\mathrm{dd22}} & S_{\mathrm{dc21}} & S_{\mathrm{dc22}} \\ S_{\mathrm{cd11}} & S_{\mathrm{cd12}} & S_{\mathrm{cc11}} & S_{\mathrm{cc12}} \\ S_{\mathrm{cd21}} & S_{\mathrm{cd22}} & S_{\mathrm{cc21}} & S_{\mathrm{cc22}} \end{bmatrix} \tag{8.1}$$

where

- $S_{\mathrm{dd}ij}$ is the differential-mode reflection/transmission parameter at logical port i when the logical port j is excited with a differential-mode signal.
- $S_{\mathrm{cc}ij}$ is the common-mode reflection/transmission parameter at logical port i when the logical port j is excited with a common-mode signal.

- $S_{\mathrm{cd}ij}$ is the differential-mode reflection/transmission parameter at logical port i when the logical port j is excited with a common-mode signal.
- $S_{\mathrm{dc}ij}$ is the common-mode reflection/transmission parameter at logical port i when the logical port j is excited with a differential-mode signal.

As an example, the cross-mode parameter $S_{\mathrm{cd}21}$ is defined as $\frac{b_{\mathrm{c}2}}{a_{\mathrm{d}1}}\big|_{a_{\mathrm{c}1}=a_{\mathrm{d}2}=a_{\mathrm{c}2}=0}$ in Figure 25 (a).

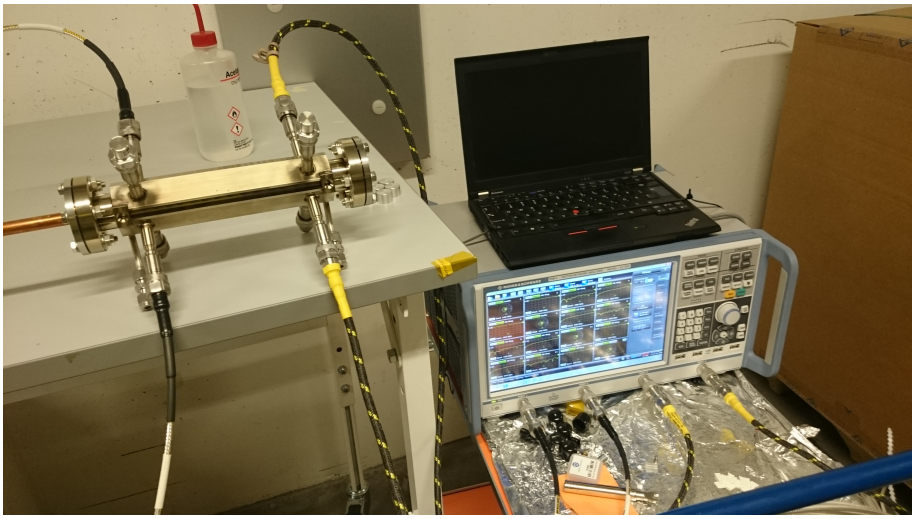

Figure 26: The test set-up during the mixed-mode S-paramater measurements.

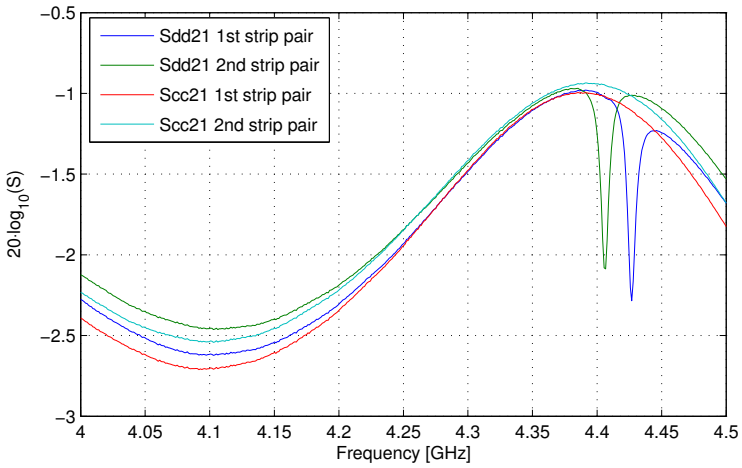

Figure 27: $S_{\mathrm{dd}21}$ and $S_{\mathrm{cc}21}$ of the two strip pairs in the range 4 to 4.5 GHz.

It is also possible to perform balanced transmission line measurement with single-ended VNA ports by using a balanced-unbalanced (*balun*) transformer network.

However, the accuracy of such measurements are limited by the phase/amplitude unbalance and by the bandwidth limitation of the network.

Two measurements per stripline are performed, where a single opposite located strip pair are characterized in each measurement. In each such measurement, the downstream stripline port of the upper strip is connected to the physical VNA port 1, while the upstream stripline port is connected to the the physical VNA port 2. Consequently, the downstream and upstream port of the lower strip are connected to the physical VNA ports 3 and 4, respectively. The four ports of the stripline pair that are not measured are terminated with 50 Ω loads. The test set-up is shown in Figure 26, and Figure 25 (b) shows a diagram of the port configuration during the measurements. The mixed-mode S-parameters of the two strip pair in the stripline that is located in the 3 GeV ring are shown in Figure 36-43 in Appendix B.

As expected, the matching becomes worse at higher frequencies as shown in the differential and common-mode reflection parameters depicted in Figure 36 and 37. This can also be seen in the differential and common-mode transmission parameters in Figure 40 and 41. However, ceramic losses in the coaxial feedthroughs also increase with frequency, so impedance mismatch is not the only reason why the throughput is lower at higher frequencies. The cross-mode parameters in Figure 42 and 43 show that the phase/amplitude balance is better for the second strip pair since $S_{\mathrm{dc21}} = S_{\mathrm{dc12}} = S_{\mathrm{cd21}} = S_{\mathrm{cd12}} = 0$ if the strips would be identical and with the same dielectric losses in the feedthroughs.

Figure 27 shows S_{dd21} and S_{cc21} of the two strip pairs in the range 4 to 4.5 GHz. Note that there is a glitch found at 4.427 GHz in the otherwise quite smooth S_{dd21} curve of the first strip pair. A similar glitch is found at 4.407 GHz when measuring the second strip pair. These glitches are the resonance responses of the first trapped $\pi/2$ mode (the TE_{11} mode) pair, listed in Table 7. As mentioned, the $\pi/2$ modes are degenerate modes and exist in orthogonal pairs. However, due to mechanical tolerances, the two-plane transverse symmetry is not perfect, which seems to have resulted in a mode separation of 20 MHz. The mechanical tolerances might also explain why the measured resonance frequencies differ 1.6 % and 2.1 %, respectively from the simulated one. Also note that the response of the trapped eigenmodes can only be seen in the S_{dd21} curves, and not in the S_{cc21} curves. This indicates that the eigenmodes are dipole modes since they are only excited when the two strips pairs are fed in differential-mode. $\boldsymbol{E}_{\perp}(r)$ in Figure 23 shows why the $\pi/2$ modes can only be excited when the strips are fed in differential-mode.

The upper bandwidth limit of the VNA is 4.5 GHz, so it was not possible to map any higher order eigenmodes during the measurements of the S-parameters.

9 RF Distribution

In this section, the design and measurements of the RF feeding network for the stripline and the receiving network for the diagnostic BPM are presented. This is for the RF networks in the MAX IV 3 GeV ring when the stripline is used for tune measurements.

The feeding network distributes the RF power delivered by an amplifier to the strips. This distribution is adjusted to the plane where the excitation occurs. The receiving network combines the signals from the four BPM buttons so that the horizontal, vertical and longitudinal motions of the beam can be monitored. The control of the feeding and receiving networks are integrated into the MAX IV control system. Unlike the S-parameter measurements described in Section 8, the measurements of the feeding and receiving networks are single-ended.

9.1 Feeding Network

Basically, the feeding network consists of three 180° 2-way splitters, eight 2-way electromechanical switches, and four adjustable phase shifters (line stretchers). A circuit diagram of the feeding network can be seen in Figure 28. The control signals to the electromechanical switches are 24 V logic and are delivered by an external PLC system. A logic diagram of the two switch control signals, Sw1-2, and how they correspond to the three modes of operation can be seen in Table 8. The numbering of the output ports and the modes of operation are the same as in Table 2 and Figure 4, respectively. The logic table is selected so that all the control signals are low when exciting the beam in the diagonal mode of operation. Thus it is possible to excite the beam so that both the horizontal and vertical tunes can be measured in case of a PLC system failure.

The bandwidth and maximum input power at Port 0 are 100 MHz - 500 MHz and 200 W, respectively. These limits are set by the specifications of the splitters [13], while the electromagnetic switches and line stretchers are more broadband and can handle higher power levels. During the initial tests, it was discovered that the switches could not be placed as close to each other as planned. The reason was that they did not switch back to the "low" state after being put in the "high" state. This is most likely because there still exists a magnetic field around the electromagnet in the neighbouring switch due to magnetic remanence. This remaining magnetic field prevents a neighbouring switch from being switched back to the "low" state. This problem was eliminated by placing sheets of mu-metal (an alloy with very high permeability) between each neighbouring pair of switches in order to provide magnetic shielding. The components of the feeding network are mounted in a standard 19” rack case, see Figure 29.

The amplifier is feed by the tracking generator of the spectrum analyzer. Both the amplifier and the spectrum analyzer are placed in a cabinet room on top of the 3 GeV ring where they are protected from radiation. The feeding network is less sensitive to radiation and is therefore placed inside the enclosure of the ring, about 1 m from the stripline. Four phase matched N-type cables are connecting the feeding network to the stripline, and the short length of the cables maximizes the delivered power to the strips. The 8 coaxial terminations (4 for the feeding network and 4 for the upstream ports of the stripline) are connected via N-type cables, and their cooling flanges are attached to a water cooling pipe in order to minimize the heat exchange to the storage ring enclosure.

It would be possible to construct a simpler network with less switches by using

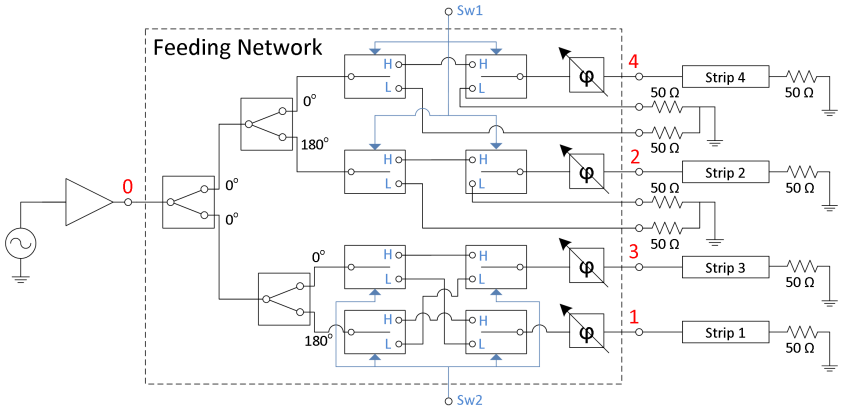

Figure 28: A circuit diagram of the stripline feeding network. The tracking generator of the spectrum analyzer is the AC source. The red numbers show the port indices during the S-parameter measurements.

Figure 29: The feeding network mounted in a standard 19" rack case. Note that half of the switches are not visible since they are shielded by sheets of mu-metal.

180° hybrid junctions as in the receiving network (see Section 9.2). However, it was decided to use a single in-house designed amplifier as the source of excitation, and we were only able to find wide-band 180° hybrid junctions that could handle much less power than the splitters used in the design described above. It would of course be possible to feed a low-power RF signal to the hybrid junctions and then add four amplifiers (one for each strip), but it would be harder to obtain a good phase and amplitude match between the four strips with this layout since the amplitude/phase unbalance between four amplifiers would be much larger than in the feeding network alone. A system with only one amplifier (and a spare unit) is also considered more reliable.

Since the amplifier is optimized for 500 MHz, the line stretchers were adjusted for that frequency. Table 9 lists the magnitudes and phases of the S_{x0} parameters at 500 MHz. The measured phase and amplitude unbalance originate mainly from

Mode of operation	Sw1	Sw2
Diagonal	L	L
Horizontal	H	L
Vertical	H	H

Table 8: The PLC logic diagram of the three modes of operation of the feeding network. Here, H (High) and L (Low) correspond to 24 V and 0 V, respectively.

the splitters. The complete S-parameters measurement results are presented in Appendix C.

	Diagonal		Horizontal		Vertical	
Port, x	$20{\cdot}\log_{10}(S_{x0})$	$\arg(S_{x0})$	$20{\cdot}\log_{10}(S_{x0})$	$\arg(S_{x0})$	$20{\cdot}\log_{10}(S_{x0})$	$\arg(S_{x0})$
1	-7.57	-107.1°	-7.57	70.4°	-7.74	-107.3°
2	< -100	-	-7.72	-108.4°	-7.72	-108.4°
3	-7.83	70.3°	-7.83	-107.0°	-7.65	70.3°
4	< -100	-	-7.54	71.7°	-7.54	71.7°

Table 9: The magnitudes and phases of the S_{x0} parameters of the feeding network at 500 MHz when the switches are set to excite the beam in the diagonal, horizontal, and vertical plane. The port indices can be seen in Figure 28.

9.2 Receiving Network

This network produces the horizontal differential, the vertical differential, and the sum signal of the induced signals from four BPM electrodes. Basically, the receiving network consists of four 180° hybrid junctions. A circuit diagram of the network can be seen in Figure 30. The hybrid junctions have a large specified bandwidth of 2-2000 MHz [11], but S-paramter measurements show that the network can be used for monitoring signals up to at least 3.5 GHz. However, the phase and magnitude unbalance becomes worse outside the specified bandwidth. The specific signal that one wants to monitor is selected by four electromechanical switches. The switches also make sure that the two signals that are not monitored are terminated. The switches are controlled by three 24 V-logic signals (Sw1-3) that are provided by a PLC system which can be controlled from the MAX IV control system. Table 10 shows the logic diagram of the three switch signals. The components are mounted inside a standard 19" rack case seen in Figure 31. The rack case is larger than needed and is therefore prepared for future modifications such as adding low-noise amplifiers, etc. Three SMA jumpers are mounted on the front of the case, and if one wants to monitor the three different signals simultaneously, one can bypass the four switches by disconnecting the jumpers and connect the instrument(s) directly to the three outputs.

The four input ports seen in Figure 30 are connected to the output ports of the diagnostic BPM chamber which have the port indices seen in Figure 32. This diagnostic BPM chamber is located in the first achromat directly after the transport line

from the LINAC. While the standard BPM chambers in the 3 GeV ring have circular cross sections, this cross section is hexagonal. Note that there is no symmetry in the yz-plane of vacuum chamber. The reason for this is that the electron pulse that is injected has an orbit that is left of the origin in the BPM chamber, while the stored beam is centered in the chamber. The "Switch Output" port is connected to the input port of the spectrum analyzer.

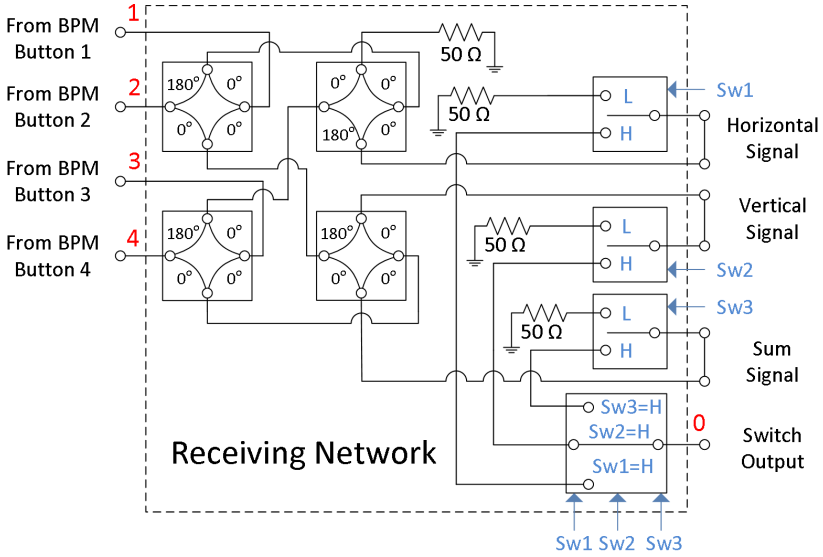

Figure 30: A circuit diagram of the receiving network. The red numbers show the port indices during the S-parameter measurements.

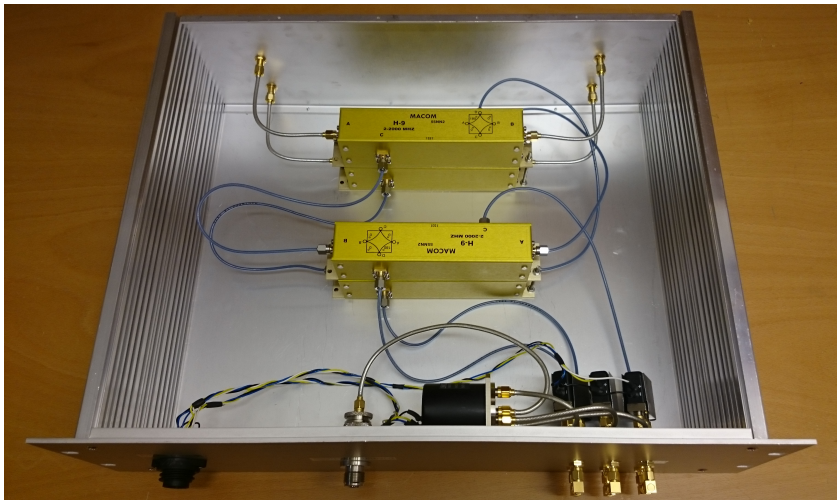

Figure 31: The receiving network mounted inside a standard 19" rack case.

Table 11 lists the magnitudes and phases of the S_{0x} parameters at 500 MHz. As seen, the measured phase and amplitude unbalance at this frequency is quite low.

Signal	Sw1	Sw2	Sw3
Horizontal	H	L	L
Vertical	L	H	L
Sum	L	L	H

Table 10: The PLC logic diagram of the receiving network when the horizontal, vertical and sum signals are monitored. Here, H (High) and L (Low) correspond to 24 V and 0 V, respectively.

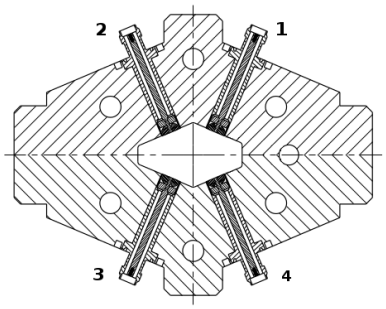

Figure 32: The 2D cross section of the diagnostic BPM chamber and the indices of the four buttons.

The complete S-parameters measurements, up to 1 GHz are presented in Appendix D.

	Horizontal		Vertical		Sum	
Port, x	$20{\cdot}\log_{10}(S_{0x})$	$\arg(S_{0x})$	$20{\cdot}\log_{10}(S_{0x})$	$\arg(S_{0x})$	$20{\cdot}\log_{10}(S_{0x})$	$\arg(S_{0x})$
1	-8.49	-17.6°	-8.31	142.9°	-8.41	-37.2°
2	-8.39	163.5°	-8.33	144.1°	-8.43	-36.0°
3	-8.41	163.5°	-8.34	-36.7°	-8.35	-37.1°
4	8.35	-15.9°	-8.36	-36.0°	-8.38	-36.2°

Table 11: The magnitudes and phases of the S_{0x} parameters of the receiving network at 500 MHz, when the switches are set to monitor the horizontal, vertical, and sum signal of the four BPM buttons. The port indices can be seen in Figure 30.

10 Initial Beam Measurements in MAX IV

Figure 33 and 34 show the power spectrum obtained at the diagnostic BPM when the stripline is exciting the beam in the horizontal and vertical plane, respectively. In each figure, the receiving network is switched to monitor the corresponding plane. The measurements were performed in the MAX IV 3 GeV ring during the initial state of beam commissioning in October 2015, and only 8 following ring buckets were filled. The total ring current during the measurements was approximately 5 mA. The peaks found at 498.51 MHz, 499.08 MHz, and 499.65 MHz are the 878:th,

879:th, and 880:th harmonic of the revolution frequency ω_0, respectively. Note that if the ring would be filled with a perfectly even filling pattern, the revolution harmonics would not be visible in the spectrum (but the RF harmonics would). The horizontal and vertical betatron oscillations can be seen as sidebands of each revolution harmonic at ± 178 kHz and ± 130 kHz, respectively.

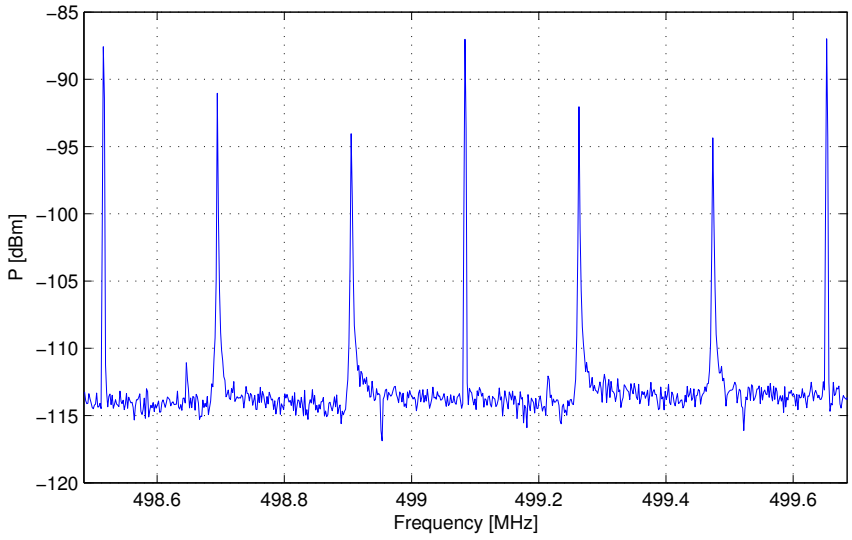

Figure 33: The power spectrum obtained at the diagnostic BPM when the beam is excited by the stripline in the horizontal plane. The peaks at 498.51 MHz, 499.08 MHz, and 499.65 MHz are harmonics of the revolution frequency. The horizontal betatron oscillations can be seen as sidebands of each revolution harmonics at ± 178 kHz.

As already mentioned in Section 2.1.2, the integer part of the betatron tunes are lost due to the stroboscope effect. Therefore, the integer parts of the tunes during the measurements were obtained by counting the number of horizontal/vertical oscillations registered by the BPM system for a distorted orbit around the ring. The horizontal and vertical integers of the tunes are 42 and 16, respectively. According to (2.6), one can not determine if the fractional part of the tunes are higher or lower than 0.5 by looking at the spectrum alone. However, by sweeping one of the quadrupole magnets and observing the tune shift, it was found that $Q_f < 0.5$ in both planes. Hence, the betatron tunes during the measurements were $Q_x = 42.31$ and $Q_y = 16.23$. These values differ somewhat from those specified in Table 1. However, the measurements were performed in the initial state of beam commissioning, and numerous adjustments have been done to the optics since.

The receiver network is switched to sum mode when monitoring the longitudinal beam motion. This is very useful when measuring the synchrotron frequency Ω_s when the phases between the accelerating cavities are adjusted. Due to the longitudinal phase focusing, the electrons inside a ring bucket reach an energy equilibrium where the mean energy gain per turn $e\hat{U}\sin(\Psi_s)$ is equal to the mean energy loss

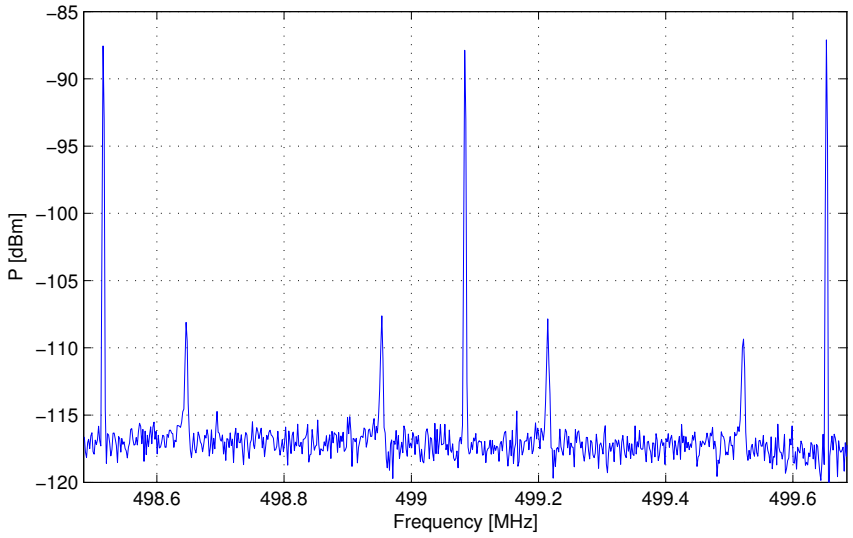

Figure 34: The power spectrum obtained at the diagnostic BPM when the beam is excited by the stripline in the vertical plane. The peaks at 498.51 MHz, 499.08 MHz, and 499.65 MHz are harmonics of the revolution frequency. The vertical betatron oscillations can be seen as sidebands of each revolution harmonics at ±130 kHz.

per turn W_0. Therefore, the relative phase of the bucket (the *synchronous phase* Ψ_s) to the fields in the accelerating cavities changes if the total peak voltage of the cavities $\hat{U}$ changes so that W_0 remains constant. Note that we define Ψ_s so that $\pi/2 < \Psi_s < \pi$ for a stored beam. The synchrotron frequency increases with the magnitude of the accelerating gradient so that $\Omega_s \propto (-\hat{U}\cos(\Psi_s))^{1/2}$. Hence, Ω_s is maximized when the fields in all the accelerating cavities have the same phase relative to the beam. Note that this relation between Ω_s, $\hat{U}$, and Ψ_s is different when the fields induced by Landau cavities are present.

Since the beam commissioning of the 3 GeV ring began in the autumn of 2015, the stripline with its RF distribution networks have been used almost on daily basis to monitor the transverse and longitudinal tunes.

11 Conclusions

In this report, the design of the striplines that are used in the MAX IV and SOLARIS storage rings is presented. The EM fields inside a stripline when the strips are excited in different modes, and their action on the beam have been analyzed. The signals that are induced at the strips by the beam via mirror currents, and their action on the beam via wakefields have also been investigated. Overall, there is a good correlation between the analysis and the simulations.

The scattering parameters of the manufactured striplines have been measured, and the result is acceptable. Two distribution networks that are feeding the stripline and selecting the plane to monitor at the diagnostic BPM have been constructed

and installed in the 3 GeV ring. The amplitude and phase balance between the ports of these networks have also been verified. Finally, initial measurements have been performed in the MAX IV 3 GeV ring where coherent transverse beam oscillations have been excited using a stripline.

Acknowledgments

We thank Jonny Ahlbäck, Eshraq Al-Dmour, Åke Andersson, Simon C. Leemann, Robert Lindvall, Magnus Sjöström, Jens Sundberg, and Pedro Fernandes Tavares for their expertise and help during the process.

Appendix A The Scalar Potential in the Stripline

The scalar potential over a cross section of the stripline is obtained by solving Laplace equation in two dimensions, cf. [9]. The analysis is here limited to the region where $0 \leq \rho \leq a$.

Since the geometry is circular, it is more convenient to use polar coordinates. Laplace equation reads

$$\nabla^2\Phi = \frac{1}{\rho}\frac{\partial}{\partial\rho}\left(\rho\frac{\partial\Phi}{\partial\rho}\right) + \frac{1}{\rho^2}\frac{\partial^2\Phi}{\partial\phi^2} = 0 \tag{A.1}$$

By using the method of separating of variables and denoting $\Phi(\rho,\phi) = R(\rho)\Psi(\phi)$, and multiplying (A.1) by ρ^2/Ψ we have

$$\frac{\rho}{R}\frac{\partial}{\partial\rho}\left(\rho\frac{\partial R}{\partial\rho}\right) + \frac{1}{\Psi}\frac{\partial^2\Psi}{\partial\phi^2} = 0 \tag{A.2}$$

The two terms in (A.2) must be constant since they are functions of ρ and ϕ respectively. If the first term equals ν^2 and the second term $-\nu^2$, the general solution becomes

$$\begin{cases} R(\rho) = c_0 + d_0\ln(\rho) + c\rho^{\nu} + d\rho^{-\nu} \\ \Psi(\phi) = C_0 + D_0\phi + Ce^{j\nu\phi} + De^{-j\nu\phi} \end{cases} \tag{A.3}$$

where the terms with indices 0 are for the special case when $\nu = 0$.

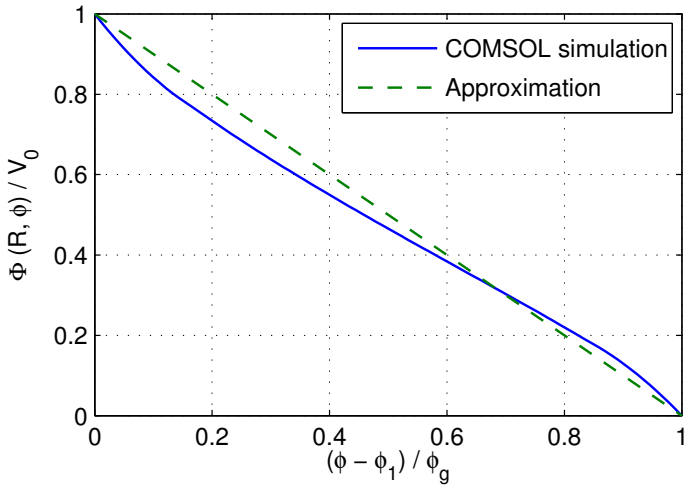

Figure 35: The simulated and approximated potential in the upper gap between the strip and the extended ground.

Consider a stripline as in Figure 4 but with only one strip that is centered at the right side with the angular extension ϕ_s and an angular gap ϕ_g to the extended ground regions. The potential of the strip is V_0 and 0 at the extended ground. The potential in the two gaps are unknown, but a good approximation is that the

azimuthal electric field is constant and the radial electric field is zero, i.e. $\boldsymbol{E}(a,\phi) = \pm\frac{V_0}{a\phi_g}\hat{\boldsymbol{\phi}}$. This implies that the potential increases/decreases linearly with ϕ in the gaps. Figure 35 shows the simulated and the approximated value of $\Phi(a,\phi)$ in the upper gap. The potential at $\rho = a$ can now be written as

$$\Phi(a,\phi) = \begin{cases} \frac{V_0}{\phi_g}(\phi_2 + \phi) & , \ -\phi_2 \leq \phi - \leq \phi_1 \\ V_0 & , \ -\phi_1 \leq \phi \leq \phi_1 \\ \frac{V_0}{\phi_g}(\phi_1 - \phi) & , \ \phi_1 \leq \phi \leq \phi_2 \\ 0 & , \text{elsewhere} \end{cases} \tag{A.4}$$

where $\phi_1 = \phi_s/2$ and $\phi_2 = \phi_s/2 + \phi_g$. Three boundary conditions can now be stated.

$$\begin{cases} (1) \text{ Full azimuthal periodicity, i.e. } \Phi(\rho,\phi) = \Phi(\rho,\phi+2\pi). \\ (2) \text{ Finite potential at the origin.} \\ (3) \ \Phi(a,\phi) \text{ as denoted in (A.4).} \end{cases}$$

(1) implies that ν is an integer, and that D_0 must vanish. d_0 and d must also vanish due to (2). $\Phi(\rho,\phi)$ can now be written as the following series

$$\Phi(\rho,\phi) = C_0 + \sum_{n=1}^{\infty} \rho^n \left(C_n e^{jn\phi} + D_n e^{-jn\phi}\right) \tag{A.5}$$

C_0 is obtained by integrating both sides over one azimuthal period when $\rho = a$.

$$\text{LHS} = \int_{-\pi}^{\pi} \Phi(a,\phi)\,\mathrm{d}\phi = V_0(\phi_1 + \phi_2)$$

$$\text{RHS} = \int_{-\pi}^{\pi} C_0\,\mathrm{d}\phi + \sum_{n=1}^{\infty} a^n \int_{-\pi}^{\pi} \left(C_n e^{jn\phi} + D_n e^{-jn\phi}\right)\mathrm{d}\phi = 2\pi C_0$$

Thus,

$$\boxed{C_0 = \frac{V_0}{2\pi}(\phi_1 + \phi_2) = \frac{V_0}{2\pi}(\phi_s + \phi_g)} \tag{A.6}$$

C_n is obtained by multiplying (A.5) by $e^{-jn'\phi}$ and then integrating over one azimuthal period when $\rho = a$.

$$
\begin{aligned}
\text{LHS} &= \int_{-\pi}^{\pi} \Phi(a,\phi) e^{-jn'\phi}\,\mathrm{d}\phi \\
&= \frac{V_0}{\phi_g}\int_{-\phi_2}^{-\phi_1} (\phi+\phi_2) e^{-jn'\phi}\,\mathrm{d}\phi + V_0 \int_{-\phi_1}^{\phi_1} e^{-jn'\phi}\,\mathrm{d}\phi + \frac{V_0}{\phi_g}\int_{\phi_1}^{\phi_2} (\phi_2-\phi) e^{-jn'\phi}\,\mathrm{d}\phi \\
&= 2V_0 \int_0^{\phi_1} \cos(n'\phi)\,\mathrm{d}\phi + \frac{2V_0\phi_2}{\phi_g}\int_{\phi_1}^{\phi_2} \cos(n'\phi)\,\mathrm{d}\phi - \frac{2V_0}{\phi_g}\int_{\phi_1}^{\phi_2} \phi\cos(n'\phi)\,\mathrm{d}\phi \\
&= \frac{2V_0}{n'}\sin(n'\phi_1) + \frac{2V_0\phi_2}{n'\phi_g}\left(\sin(n'\phi_2)-\sin(n'\phi_1)\right) \\
&\quad - \frac{2V_0}{n'\phi_g}\left(\phi_2\sin(n'\phi_2)-\phi_1\sin(n'\phi_1)\right) - \frac{2V_0}{n'^2\phi_g}\left(\cos(n'\phi_2)-\cos(n'\phi_1)\right) \\
&= \frac{2V_0}{n'^2\phi_g}\left(\cos(n'\phi_1)-\cos(n'\phi_2)\right) \\
&= \frac{4V_0}{n'^2\phi_g}\sin\left(n'\frac{\phi_g}{2}\right)\sin\left(n'\frac{\phi_s+\phi_g}{2}\right) \\
\text{RHS} &= \int_{-\pi}^{\pi} C_0 e^{-jn'\phi}\,\mathrm{d}\phi + \sum_{n=1}^{\infty} a^n \int_{-\pi}^{\pi}\left(C_n e^{j(n-n')\phi} + D_n e^{-j(n+n')\phi}\right)\mathrm{d}\phi \\
&= 2\pi\sum_{n=1}^{\infty} a^n C_n \delta_{n,n'} = 2\pi a^{n'} C_{n'}
\end{aligned}
$$

Thus,

$$
\boxed{C_n = \frac{2V_0}{\pi\phi_g} a^{-n} \frac{\sin\left(n\frac{\phi_g}{2}\right)\sin\left(n\frac{\phi_s+\phi_g}{2}\right)}{n^2}} \tag{A.7}
$$

D_n is obtained in the same way as C_n, except by multiplying both side in (A.5) by $e^{jn'\phi}$ instead of $e^{-jn'\phi}$. Due to symmetry, we have that

$$
\boxed{D_n = C_n} \tag{A.8}
$$

By inserting (A.6), (A.7), and (A.8) into (A.5), $\Phi(\rho,\phi)$ can finally be written as

$$
\Phi(\rho,\phi) = \frac{V_0(\phi_s+\phi_g)}{2\pi} + \frac{4V_0}{\pi\phi_g}\sum_{n=1}^{\infty}\left(\frac{\rho}{a}\right)^n \frac{\sin\left(n\frac{\phi_g}{2}\right)\sin\left(n\frac{\phi_s+\phi_g}{2}\right)}{n^2}\cos(n\phi) \tag{A.9}
$$

We can now calculate the potential for an arbitrary rotated strip by adding its rotation angle α to (A.9), thus $\cos(n\phi) \to \cos(n(\phi-\alpha))$. We superimpose the

potentials from the four strips, and the potential of the excitation modes listed in Table 2 can be written as

$$\Phi(\rho,\phi) = \sum_{m=1}^{4} \frac{U_m}{\pi} \left(\frac{\phi_s + \phi_g}{2} + \frac{4}{\phi_g} \sum_{n=1}^{\infty} \left(\frac{\rho}{a}\right)^n \frac{\sin\left(n\frac{\phi_g}{2}\right) \sin\left(n\frac{\phi_s+\phi_g}{2}\right)}{n^2} \cos\left(n\left(\phi - \frac{m\pi}{2} + \frac{\pi}{4}\right)\right) \right)$$

where U_m is the potential of the m:th electrode.

Appendix B Stripline S-parameter Measurement

The S-parameters from the measurements described in Section 8 can be seen in Figure 36-43. Here, all the 2x16 parameters are not shown since $S_{\mathrm{dc11}} \approx S_{\mathrm{cd11}}$, $S_{\mathrm{dc22}} \approx S_{\mathrm{cd22}}$, $S_{\mathrm{dd21}} \approx S_{\mathrm{dd12}}$, and $S_{\mathrm{cc21}} \approx S_{\mathrm{cc12}}$.

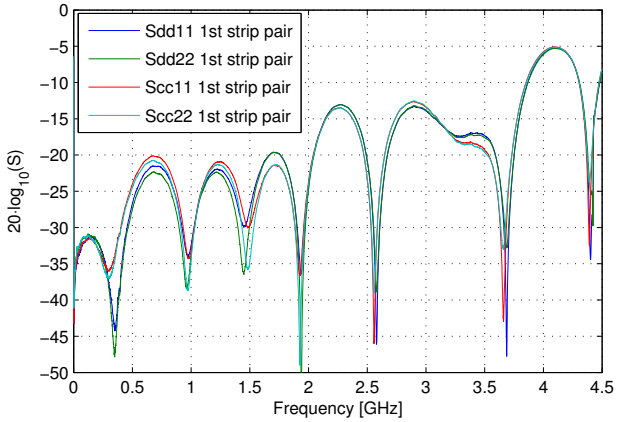

Figure 36: Differential and common-mode reflection coefficients of the first strip pair.

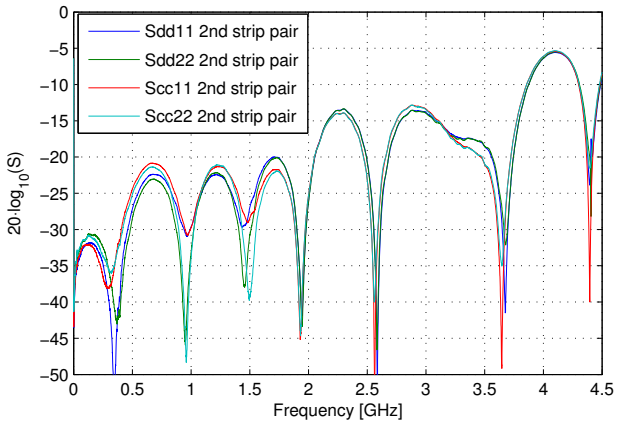

Figure 37: Differential and common-mode reflection coefficients of the second strip pair.

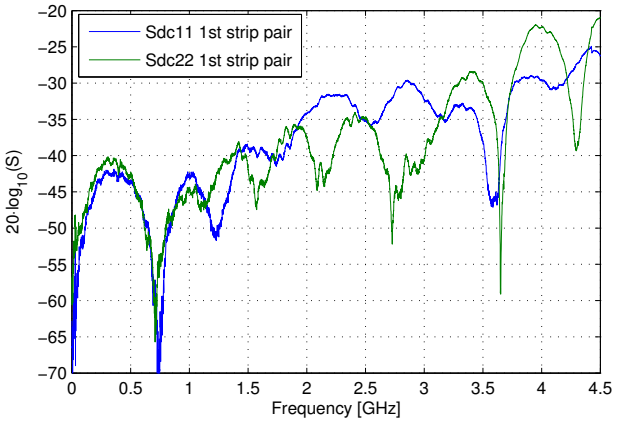

Figure 38: Cross-mode reflection coefficients of the first strip pair.

Figure 39: Cross-mode reflection coefficients of the second strip pair.

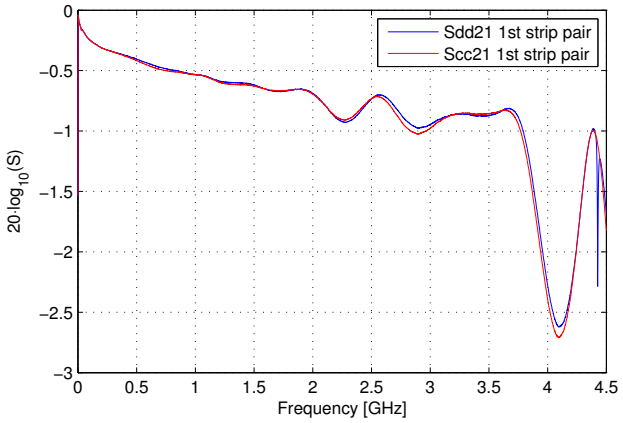

Figure 40: Differential and common-mode transmission coefficients of the first strip pair.

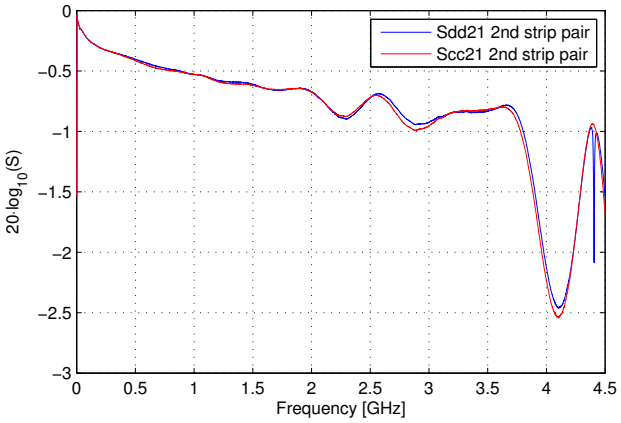

Figure 41: Differential and common-mode transmission coefficients of the second strip pair.

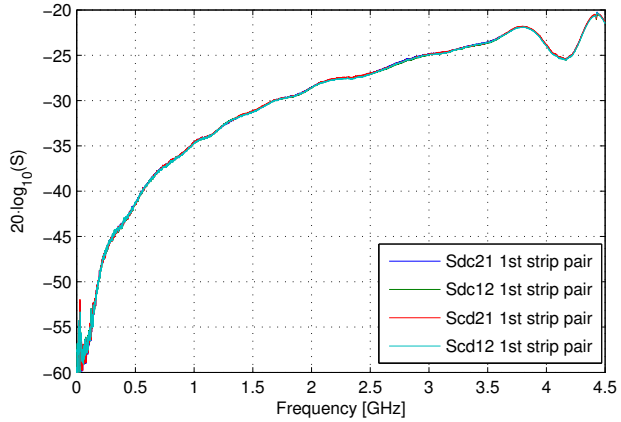

Figure 42: Cross-mode transmission coefficients of the first strip pair.

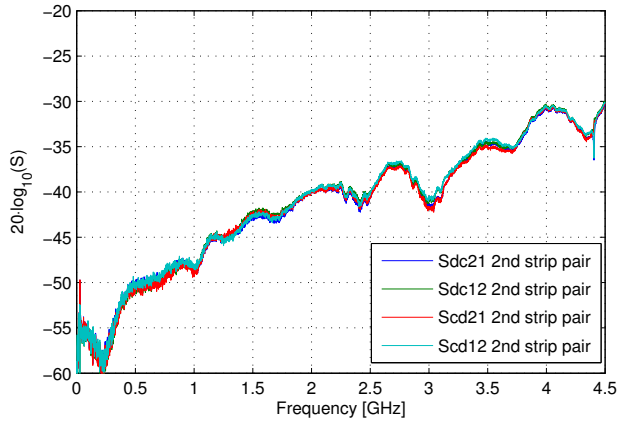

Figure 43: Cross-mode transmission coefficients of the second strip pair.

Appendix C Feeding Network S-parameter Measurements

Here, the S-parameter measurements of the feeding network in Section 9.1 are presented. The port numbering in Figure 28 are used. The transmission coefficients of the network can be seen in Figure 44-49, and Figure 50 shows S_{00}.

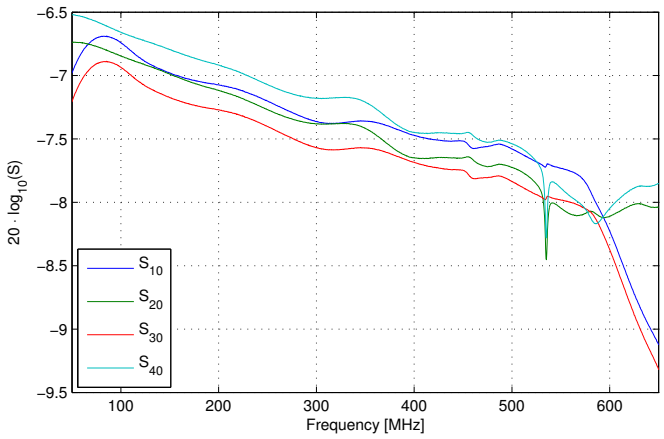

Figure 44: S_{x0} of the feeding network in the horizontal mode.

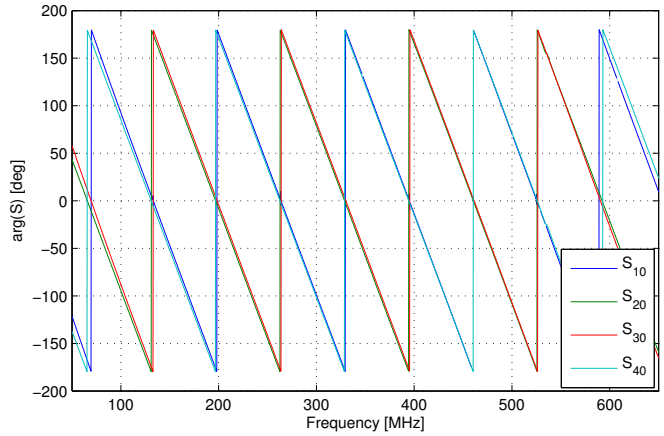

Figure 45: S_{x0} of the feeding network in the horizontal mode.

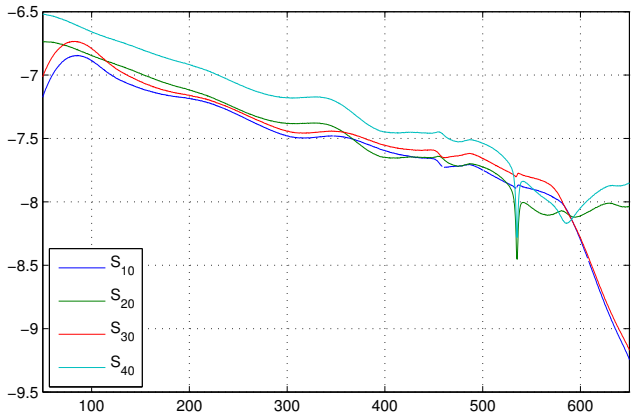

Figure 46: S_{x0} of the feeding network in the vertical mode.

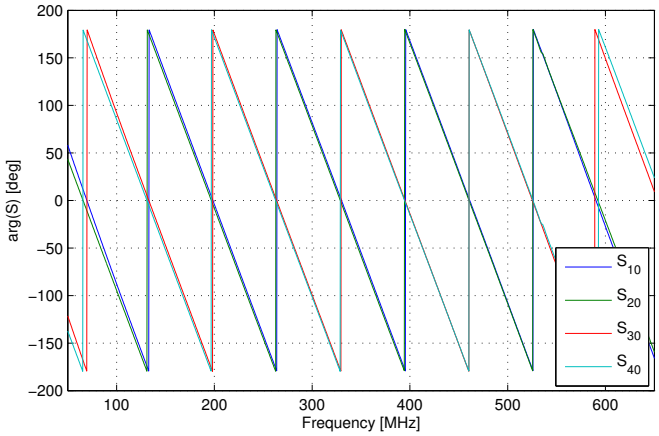

Figure 47: S_{x0} of the feeding network in the vertical mode.

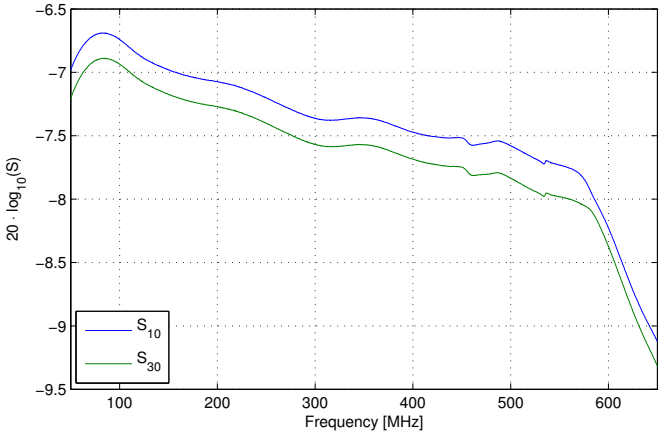

Figure 48: S_{x0} of the feeding network in the diagonal mode.

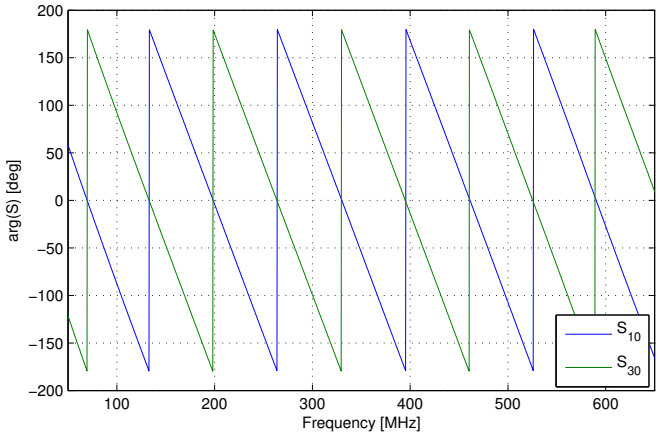

Figure 49: S_{x0} of the feeding network in the diagonal mode.

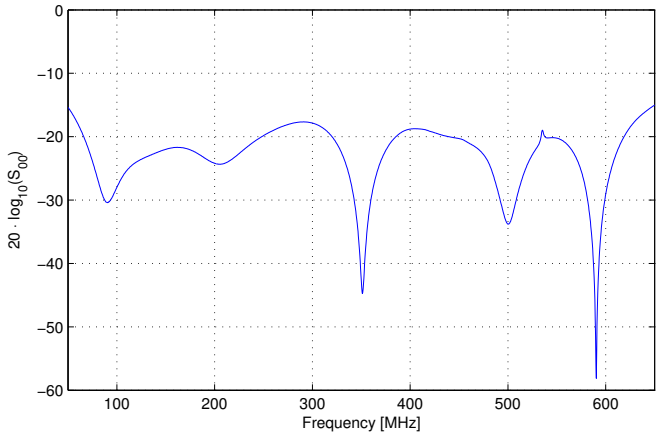

Figure 50: S_{00} of the feeding network in the diagonal mode. Note that S_{00} does not differ much in the horizontal and vertical mode of operation.

Appendix D Receiving Network S-parameter Measurements

Here, the S-parameter measurements of the receiving network in Section 9.2 are presented. The four input ports can be seen in Figure 30 and correspond to the button indices in Figure 32. Port 0 is the "Switch Output" port in Figure 30. The spectrum of the transmission coefficients can be seen in Figure 51-56.

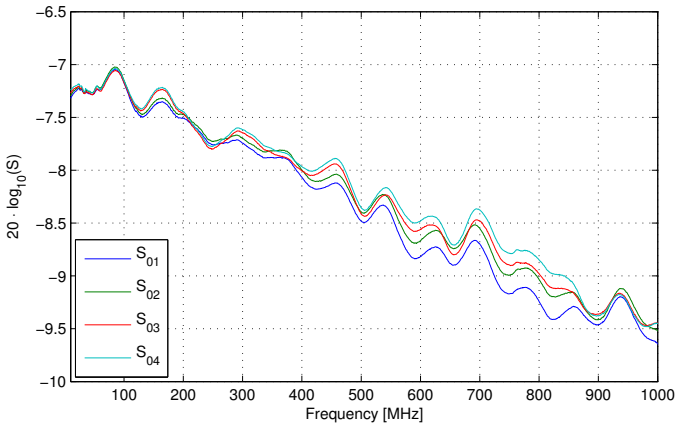

Figure 51: S_{0x} of the receiving network when monitoring the horizontal signal.

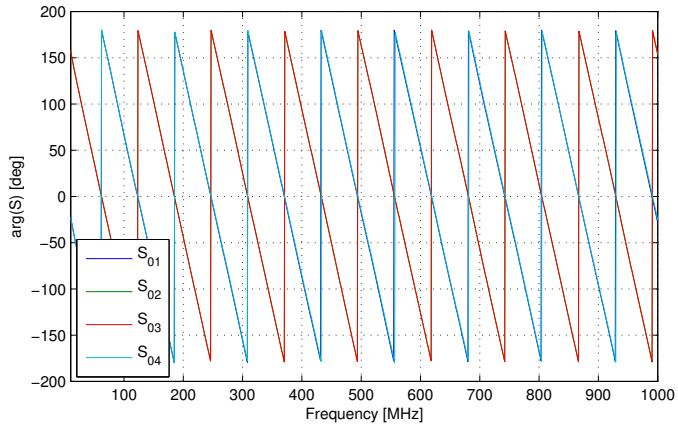

Figure 52: S_{0x} of the receiving network when monitoring the horizontal signal.

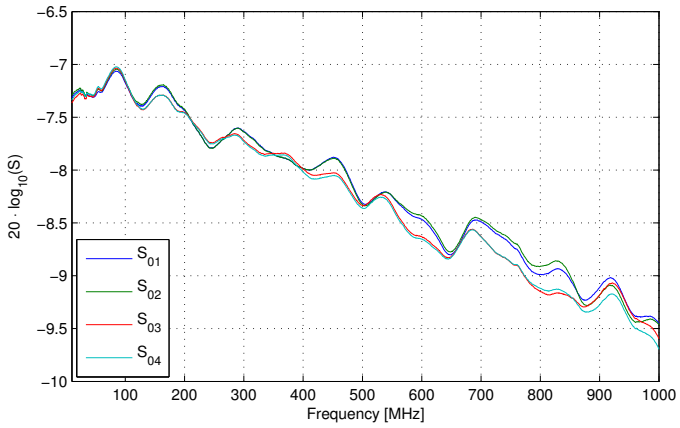

Figure 53: S_{0x} of the receiving network when monitoring the vertical signal.

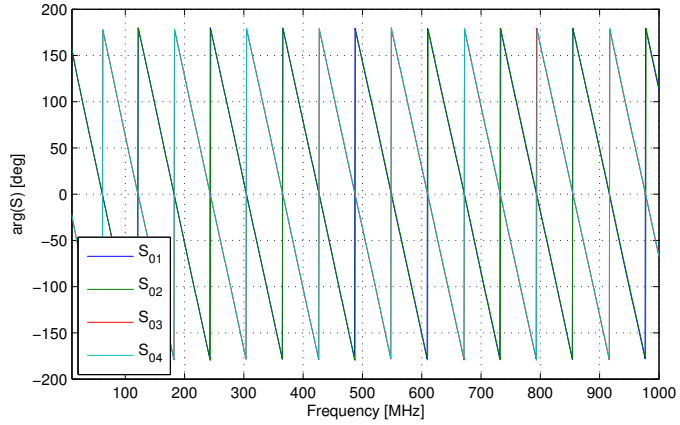

Figure 54: S_{0x} of the receiving network when monitoring the vertical signal.

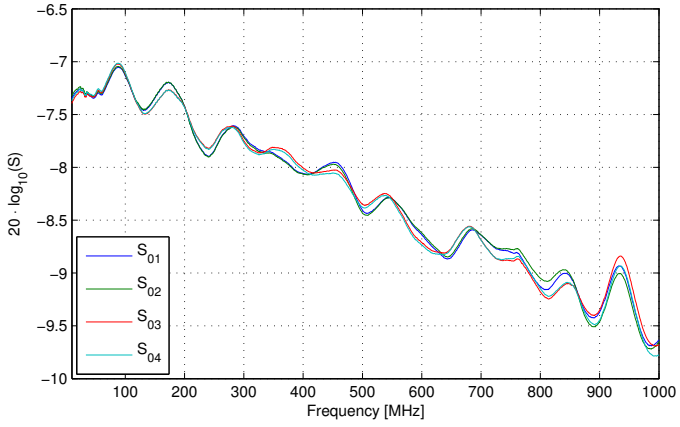

Figure 55: S_{0x} of the receiving network when monitoring the sum signal.

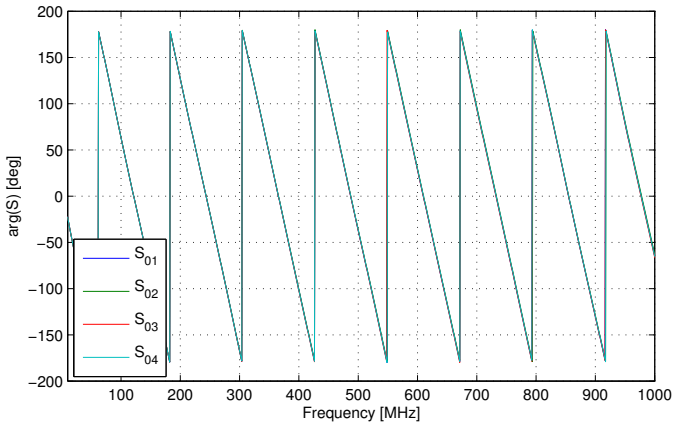

Figure 56: S_{0x} of the receiving network when monitoring the sum signal.

Appendix References

[1] Å. Andersson et al. "The 100 mhz rf system for the max iv storage rings". In: *2nd International Particle Accelerator Conference*. 2011, pp. 193–195.

[2] *COMSOL Multiphysics website.* http://www.comsol.com.

[3] F. Curbis et al. "Extension of the max iv linac for a free electron laser in the x-ray region". In: *International Particle Accelerator Conference (IPAC), Shanghai, China*. 2013, pp. 1244–1246.

[4] *GdfidL website.* http://www.gdfidl.de.

[5] A. S. Gilmour. *Klystrons, Traveling Wave Tubes, Magnetrons, Crossed-Field Amplifiers, and Gyrotrons*. Artech House, 2011.

[6] D. A. Goldberg and G. R. Lambertson. "Dynamic devices a primer on pickups and kickers". In: *AIP Conference Proceedings*. 1992, pp. 537–600.

[7] M. Hiebel. *Fundamentals of Vector Network Analysis*. Rohde&Schwarz GmbH & Co, 2008.

[8] A. Hofmann and S. Myers. "Beam dynamics in a double rf system". In: *11th International Conference on High-energy Accelerators*. 1980, pp. 610–614.

[9] J. D. Jackson. *Classical Electrodynamics*. Third. John Wiley & Sons, 1999.

[10] A. Karlsson and G. Kristensson. *Mikrovågsteori*. KFS AB, 2003.

[11] *MACOM H-9 180° hybrid junction product specifications.* http://cdn.macom.com/datasheets/H-9.pdf.

[12] *MAX IV Laboratory website.* https://www.maxlab.lu.se/maxiv.

[13] *MCLI splitter product specifications.* http://mcli.com/documents/hcd-12.pdf http://mcli.com/documents/hcd-19.pdf.

[14] K. Y. Ng. "Impedance of stripline beam-position monitors". *Particle Accelerators* 23 (1988), pp. 93–102.

[15] D. Olsson. "Design of stripline kicker for tune measurements in the max iv 3 gev ring". In: *Progress In Electromagnetics Research Symposium Proceedings (PIERS)*. 2013, pp. 1095–1099.

[16] D. Olsson, A. Karlsson, and L. Malmgren. *The Bunch-by-Bunch Feedback System in the MAX IV 3 GeV Ring*. Tech. rep. LUTEDX/(TEAT-7253)/(2017). Lund Institute of Technology, 2017.

[17] D. Olsson et al. "A chopper system for the max iv thermionic pre-injector". *Nuclear Instruments and Methods in Physics Research* 759 (2014), pp. 29–35.

[18] M. Serio. "Transverse betatron tune measurements". *Frontiers of Particle Beams; Observation, Diagnosis and Correction Lecture Notes in Physics* 343 (1989), pp. 65–93.

[19] *SOLARIS Synchrotron website.* http://www.synchrotron.uj.edu.pl.

[20] P. F. Tavares et al. “The max iv storage ring project”. *Journal of Synchrotron Radiation* 21 (2014), pp. 862–877.

[21] S. Thoorin et al. “Design of the max iv ring injector and spf/fel driver”. In: *Particle Accelerator Conference (PAC), New York, NY, USA*. 2011, pp. 2447–2449.

[22] H. Wiedemann. *Particle Accelerator Physics*. Third. Springer-Verlag, 2007.

[23] K. Wille. *The Physics of Particle Accelerators*. Oxford University Press, 2000.

[24] B. W. Zotter and S. Kheifets. *Impedances and Wakes in High-Energy Particle Accelerators*. World Scientific Publisher, 1998.